
Electronic Theses and Dissertations, 2004-2019

2013

Automated Hybrid Singularity Superposition And Anchored Grid Pattern Bem Algorithm For The Solution Of The Inverse Geometric Problem

Marcus Ni
University of Central Florida



Part of the [Mechanical Engineering Commons](#)

Find similar works at: <https://stars.library.ucf.edu/etd>

University of Central Florida Libraries <http://library.ucf.edu>

This Masters Thesis (Open Access) is brought to you for free and open access by STARS. It has been accepted for inclusion in Electronic Theses and Dissertations, 2004-2019 by an authorized administrator of STARS. For more information, please contact STARS@ucf.edu.

STARS Citation

Ni, Marcus, "Automated Hybrid Singularity Superposition And Anchored Grid Pattern Bem Algorithm For The Solution Of The Inverse Geometric Problem" (2013). *Electronic Theses and Dissertations, 2004-2019*. 2669.

<https://stars.library.ucf.edu/etd/2669>

AUTOMATED HYBRID SINGULARITY SUPERPOSITION AND
ANCHORED GRID PATTERN BEM ALGORITHM FOR THE SOLUTION OF
THE INVERSE GEOMETRIC PROBLEM

by

MARCUS W. NI
B.S. University of Central Florida, 2012

A thesis submitted in partial fulfillment of the requirements
for the degree of Master of Science
in the Department of Mechanical, Materials and Aerospace Engineering
in the College of Engineering and Computer Science
at the University of Central Florida
Orlando, Florida

Summer Term
2013

ABSTRACT

A method for solving the inverse geometrical problem is presented by reconstructing the unknown subsurface cavity geometry using boundary element methods, a genetic algorithm, and Nelder-Mead non-linear simplex optimization. The heat conduction problem is solved utilizing the boundary element method, which calculates the difference between the measured temperature at the exposed surface and the computed temperature under the current update of the unknown subsurface flaws and cavities. In a first step, clusters of singularities are utilized to solve the inverse problem and to identify the location of the centroid(s) of the subsurface cavity(ies)/flaw(s). In a second step, the reconstruction of the estimated cavity(ies)/flaw(s) geometry(ies) is accomplished by utilizing an anchored grid pattern upon which cubic spline knots are restricted to move in the search for unknown geometry. Solution of the inverse problem is achieved using a genetic algorithm accelerated with the Nelder-Mead non-linear simplex. To optimize the cubic spline interpolated geometry, the flux (Neumann) boundary conditions are minimized using a least squares functional. The automated algorithm successfully reconstructs single and multiple subsurface cavities within two dimensional mediums. The solver is also shown to accurately predict cavity geometries with random noise in the boundary condition measurements. Subsurface cavities can be difficult to detect based on their location. By applying different boundary conditions to the same geometry, more information is supplied at the boundary, and the subsurface cavity is easily detected despite its low heat signature effect at the boundaries. Extensions to three-dimensional applications are outlined.

ACKNOWLEDGMENTS

First and foremost, I would like to thank Dr. Alain J. Kassab for all his guidance and knowledge in the field of heat transfer and boundary elements. Without his guidance, this paper would not have been possible, and I would never have accomplished such a great academic achievement. I would also like to thank Dr. Eduardo Divo for sharing his research and techniques for shape optimization. Dr. Divo's knowledge of algorithm code writing has helped me to create this automated system work quickly and flawlessly.

TABLE OF CONTENTS

INTRODUCTION	1
SOLUTION PROCEDURE.....	5
The forward problem solver: Boundary element method	5
Geometry reconstruction: Cubic spline interpolation	7
Geometry optimization technique: Nelder-Mead simplex.....	9
NUMERICAL EXAMPLES.....	14
Case 1: Boundary element method testing.....	14
Case 2: Source and high resolution testing	15
Case 3: Cavity detection testing.....	17
Case 4: Geometry reconstruction testing	21
Case 5: Single cavity reconstruction experiment.....	23
Case 6: Single cavity reconstruction with noisy measurements experiment	28
Case 7: Multiple cavity reconstruction experiment	31
Case 8: Notch cavity reconstruction experiment	35
Case 9: Multiple boundary condition set optimization	37
Case 10: MBCS using environmentally realistic boundary conditions	39
CONCLUSION.....	42
REFERENCES	43

LIST OF FIGURES

Figure 1: Problem setup using IR scanner to measure thermal footprint at the exposed boundary. Image provided by E. Divo et al [2]	2
Figure 2: Cubic spline interpolation representation.....	8
Figure 3: Left - graphical representation of logic employed to keep AGP points within medium. Right - point located beyond the medium.....	11
Figure 4: Multiple boundary conditions sets experiment	13
Figure 5: Case 1 geometry of hexagon with two cavities.....	14
Figure 6: Case 1 analysis of error in flux calculations using BEM	15
Figure 7: Case 2 geometry of annulus with source locations	16
Figure 8: Case 2 analysis of error in flux calculations using BEM	16
Figure 9: Case 3 first guess source locations	17
Figure 10: Case 3 third iteration source locations	18
Figure 11: Case 3 twentieth iteration source locations	18
Figure 12: Case 3 final solution source locations	19
Figure 13: Case 3 temperature field with source term of final solution	20
Figure 14: Case 3 heat flow magnitude with source term of final solution.....	20
Figure 15: Case 4 initial guess of cavity geometry.....	21
Figure 16: Case 4 intermediate iteration of cavity geometry.....	22
Figure 17: Case 4 final solution of cavity geometry.....	22
Figure 18: Case 5 geometry and initial guess locations.....	24
Figure 19: Case 5 optimization process 50% complete	24

Figure 20: Case 5 optimization process 75% complete	25
Figure 21: Case 5 final solution, no noise in measurements.....	25
Figure 22: Case 5 initial guess temperature plot.....	26
Figure 23: Case 5 final solution temperature plot.....	27
Figure 24: Case 5 initial guess heat flow magnitude plot.....	27
Figure 25: Case 5 final solution heat flow magnitude plot.....	28
Figure 26: Case 6 with 1% noise in flux boundary conditions	29
Figure 27: Case 6 with 2% noise in flux boundary conditions	30
Figure 28: Case 6 with 1% noise in both the temperature and flux boundary conditions	30
Figure 29: Case 7 initial guess of two cavity 80 parameter optimization.....	31
Figure 30: Case 7 final solution of 80 parameter optimization	32
Figure 31: Case 7 geometry and boundary conditions.....	33
Figure 32: Case 7 final solution of 16 parameter optimization	34
Figure 33: Case 7 convergence plot of 16 parameter optimization	34
Figure 34: Case 8 experimental setup one	35
Figure 35: Case 8 final solution to the notch cavity search using one set of boundary conditions	36
Figure 36: Antennae pattern anchored grid pattern concept.....	36
Figure 37: Case 9 experimental setup two.....	37
Figure 38: Case 9 final solution to the notch cavity using multiple boundary condition sets when optimizing the cavity parameters	38
Figure 39: Case 10 boundary condition setup.....	39

Figure 40: Case 10 two set MBCS optimization solution.....	41
Figure 41: Case 10 four set MBCS optimization solution.....	41

INTRODUCTION

Forward problems are defined as well posed, and require five specifications which are as follows: governing equation for field variable, physical properties, boundary conditions, initial condition(s) and system geometry [2], [13], [14]. The inverse geometrical problem is one of many inverse problems that arise in engineering today. This problem is broadly classified into the inverse problem category. The inverse problem differs from the forward problem in that one of the forward problem specifications is unknown, and there is at least one over specified condition. In most cases, including the inverse geometric problem, this over specified condition arises at the boundary, which lends itself to the boundary element method (BEM).

Subsurface cavity detection and geometry reconstruction methods using BEM have been well documented within the past decade [1], [3]. These methods are non- intrusive, and have been successfully proven to detect sub surface cavities, as well as predict its shape. In these problems the governing equation, physical properties, boundary conditions, initial conditions and external geometry are known, leaving the internal cavity wall geometry unknown. The boundary conditions at the cavity walls are also considered to be known as adiabatic, or very close to adiabatic. This can be attributed to the extremely low thermal conductivity of the material or void within the cavity. Radiation would have an effect on these subsurface cavity boundary conditions at high temperatures, however, has been omitted because the temperature ranges should be kept relatively low.

An efficient way to detect cavity shape and location was proposed by E. Divo in 2004 [2]. In his article the inverse geometric problem is stated much like the one in this article, and the use of point source clusters is employed to search for subsurface cavities in 2-D and 3-D

geometries by minimizing the first order boundary condition at the exposed surface. The efficiency of his model comes from lack of grid reconstruction. Rather than actually reconstructing the cavity walls during the optimization, a search for the adiabatic condition is run with the optimized cluster location and shape in place to act as the void within the medium. The shape is simplified to be elliptical to lower optimization parameters, and the technique has proven to be successful. Application of these techniques requires thermal imaging of the exposed surface with the use of infrared scanners as shown in Figure 1. At this point the boundary conditions at the exposed surface are over specified, and the internal cavity location and shape is unknown.

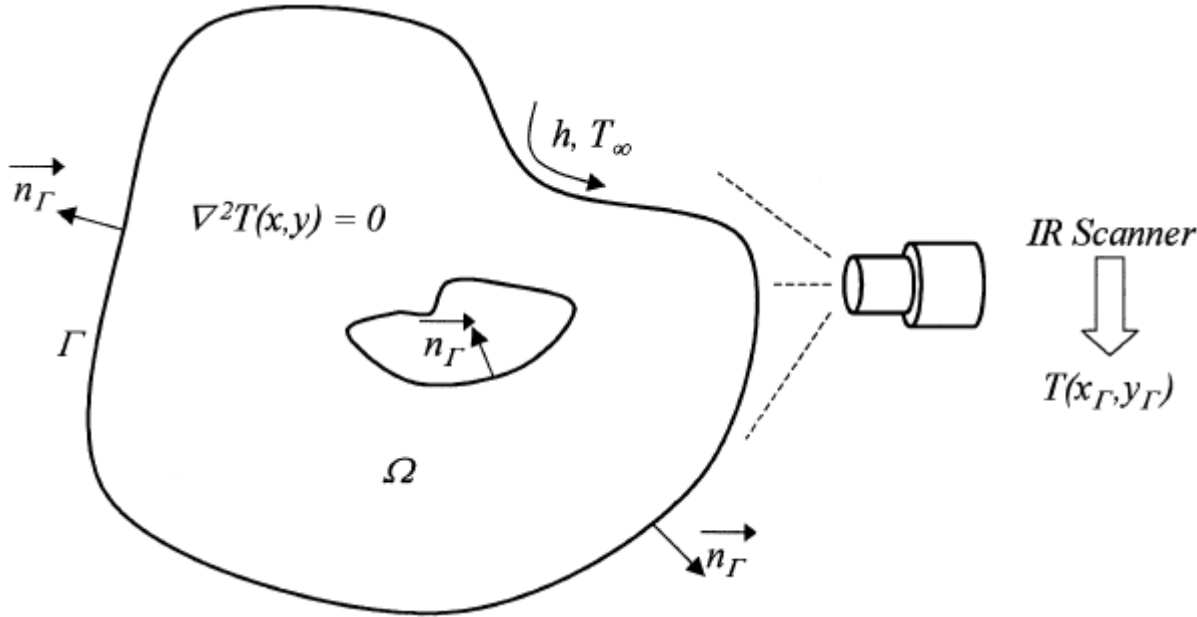


Figure 1: Problem setup using IR scanner to measure thermal footprint at the exposed boundary. Image provided by E. Divo et al [2]

It is also possible to utilize elastics rather than heat conduction to search for these cavities. Kassab et al [3] present a solution using elastostatics and the boundary element method.

Rather than minimizing the Neumann or Cauchy boundary conditions of the heat transfer problem, the strains and deformations at the exposed surface boundaries are minimized. This paper also proposes a variety of differently shaped anchored grid patterns (AGP) that adapt to the shape of the internal cavity [3].

Another solution to this inverse problem is to use the method of fundamental solutions (MFS) rather than the boundary element method (BEM), proposed by A. Karageorghis [5]. In one these methods, Karageorghis utilizes a moving pseudo-boundary technique to detect void location and boundary location. The heat conduction equation and Neumann boundary condition minimization are also utilized similar to this articles approach. High resolution of these cavity boundaries are obtained by using radial polar parameterization, which simply searches for points radially around the cavity center [5], [8]. This technique causes high number of parameters to be optimized which can lead to longer calculation times and instability. Karageorghis also proposed a solution to cavity detection within plane linear elastic bodies. The same MFS and radial polar parameterization technique is used; however, the boundary conditions to be minimized are described by the elastic properties of the medium. Boundary deformity, strain, levels are minimized to optimize the cavity location and shape [7].

In this thesis, a higher resolution algorithm for cavity shape is proposed by using an anchored grid pattern to map a cubic spline that wraps itself around the cavity. The boundary element method is used to solve the forward heat transfer problem at each step of the overall inverse problem that in turn employs simplex optimization techniques. First, the boundary element method code developed for this thesis is validated by using simple tests involving the encompassing general heat conduction equation. Since the problem at hand involves the use of

heat signatures, the conduction equation is used and reduced to the Laplace equation due to the steady state and constant property assumptions. A temperature field that satisfies the Laplace equation is imposed, and the method is validated by matching exterior and interior points of temperature and heat flow. In essence, the boundary element calculations are being compared to the analytical Laplace equation solution for the test problems. This simple approach can also be used to check point source influences by using the same procedure, except the general equation is now non-homogeneous.

The automated algorithm for reconstruction of cavity geometry starts by searching for its general location using clusters of sources/sinks that satisfy the heat flux (Neumann) boundary conditions. These cluster(s) must locate themselves within the cavity or outside of the medium to satisfy the Laplace equation. The boundary element method is used to solve the forward problem, while the simplex method optimizes the location of these source/sink clusters. Once the cavity location is determined, the same steps are used to predict the geometry's shape using cubic spline interpolation. By using an anchored grid pattern, the cavity is shaped using eight splines, to which the surface is attached [1]. This pattern is placed at the center of the detected cavity, adiabatic boundary conditions are applied to this cubic spline surface, and the spline lengths are optimized to satisfy the heat flux (Neumann) boundary conditions. This application has also been extended to include multiple cavities, and unknown subsurface boundary conditions. This study has been successful in adding shape resolution to the *Efficient Singularity Super Position Technique* [2], and should be extended to 3-D geometries using these same techniques. The concept of multiple boundary condition set (MBCS) optimization was also used to effectively to enhance sensitivity and detect complicated geometrical shapes and locations.

SOLUTION PROCEDURE

To begin to understand the solution to the geometric problem, a layout for the automated algorithm is presented. First, the forward problem is solved using boundary elements with the source/sink clusters to imitate subsurface cavity behavior. Second, the clusters are moved to the cavity location with the help of the genetic algorithm method. Once the cavity is located, an anchored grid pattern replaces the clusters, and a new surface is created to guess at the cavity geometry. These anchored grids are then optimized with the Nelder-Mead simplex method until the Neumann boundary conditions, that have been over specified, agree with the boundary element solution.

- 1) Set up problem parameters and initial guesses for the cavity location
- 2) Solve forward problem using BEM
- 3) Optimize the cavity location using the genetic algorithm
- 4) Use optimized location for central spline knot of cubic interpolation and set up initial guesses for the cavity geometry
- 5) Solve forward problem using BEM
- 6) Optimize the cavity geometry using the Nelder-Mead simplex

The forward problem solver: Boundary element method

As stated previously, the general equation to be solved is the homogeneous Laplace equation, equation 1, where T is the temperature at the point (x, y) with in the medium Ω .

$$\nabla^2 T(x, y) = 0 \text{ in } \Omega \quad (1)$$

The boundary element method solves for $T(x, y)$ numerically by discretizing the boundary into several elements. Green's second identity is applied and a free space test function, T^* , is introduced to the Laplace equation. It is then integrated over the surface elements, Γ , as shown in equation 2 [8].

$$C(i)T(i) + \sum_{j=1}^N \oint_{\Gamma_j} T q^* d\Gamma = \sum_{j=1}^N \oint_{\Gamma_j} T^* q d\Gamma \text{ where } q^* = dT^* \quad (2)$$

The temperature for the given point “i” has been solved by integrating over the surface elements labeled “j”, where N is the number of surface elements. “C” is termed the jump coefficient, which is determined as 0.5 for completely smooth elements. Since T and q are constant over the element, they are taken out of the integral, and the test functions are labeled accordingly as shown in equations 3 and 4.

$$H_{ij} = \oint_{\Gamma_j} q^* d\Gamma \quad (3)$$

$$G_{ij} = \oint_{\Gamma_j} T^* d\Gamma \quad (4)$$

Once the elements have been discretized, equation 2 can be written in the standard form as equation 5 [8].

$$\sum_{j=1}^N G_{ij} q_j = \sum_{j=1}^N H_{ij} T_j \quad (5)$$

This formulation does not take into consideration point sources, however, the point sources can be simply added to the right hand side of this equation. Equation 6 shows the added point sources to the general equation, where {B} is the source vector shown in equation 7 [12].

$$[G]\{q\} = [H]\{T\} + \{B\} \quad (6)$$

$$B_i = \sum_{j=1}^{N_s} \frac{Q_j}{2\pi} * \frac{1}{2} * [(x_i - x_j)^2 + (y_i - y_j)^2] \quad (7)$$

The standard procedure to solve equation 6 is to move all the unknown boundary conditions to the same vector and use matrix multiplication to simplify. This simplification leads to equation 8, and is easily solved using pivoting methods for multiple sets of equations.

$$[A]\{x\} = \{b\} \quad (8)$$

The solution for “{x}” represents the unknown boundary conditions that are being solved for. Using this solution and equation 2 the entire solution is formed.

Geometry reconstruction: Cubic spline interpolation

To reconstruct the subsurface cavity geometry, a cubic spline interpolator generates a surface around a central point provided by the efficient hole finding optimization [2]. The first step is to define the anchored pattern as to which the cubic splines will attach themselves. Eight splines are defined to be positive, be equally separated and extend from the central knot as shown in Figure 2. The ends of these splines define the cubic spline endpoints, and continuity conditions define the shape. Since the angles between each spline are fixed and the shape is periodic, polar coordinates are used to define the locations along the cubic splines. According to Pollard and Kassab [1], the location along the cubic spline surface can be defined by equation 9,

$$r(\theta) = M_{i-1} \frac{(\theta_i - \theta)^3}{6\Delta\theta_i} + M_i \frac{(\theta - \theta_{i-1})^3}{6\Delta\theta_i} + \left(r_{i-1} - \frac{M_{i-1}\Delta\theta_i^2}{6} \right) \frac{\theta_i - \theta}{\Delta\theta_i} + \left(r_i - \frac{M_i\Delta\theta_i^2}{6} \right) \frac{\theta - \theta_{i-1}}{\Delta\theta_i} \quad (9)$$

where “r” is the radial position along the polar coordinate system which depends on “θ”, the angle along the polar coordinate system. The “i” corresponds to the intervals between each spline, adding up to eight in this case. The spacing between each spline is defined as $\Delta\theta_i = \theta_i - \theta_{i-1}$, which is considered to be fixed in these problems. The continuity conditions, mentioned previously, state that the first and second derivatives at the spline endpoints are continuous from interval to interval. The periodic condition states that the first location is equal

to the last location. These conditions lead to a set of tri-diagonal equations shown in equation 10, 11 and 12. This simple set of equations is solved during the optimization using the Thomas algorithm.

$$2M_1 + \lambda M_2 = d_1 \quad (10)$$

$$\mu_i M_{i-1} + 2M_i + \lambda_i M_{i+1} = d_i \quad i = 2, 3, \dots, 7 \quad (11)$$

$$\mu_8 M_7 + 2M_8 = d_8 \quad (12)$$

The coefficients are defined by Pollard and Kassab's cubic spline anchored grid pattern [1].

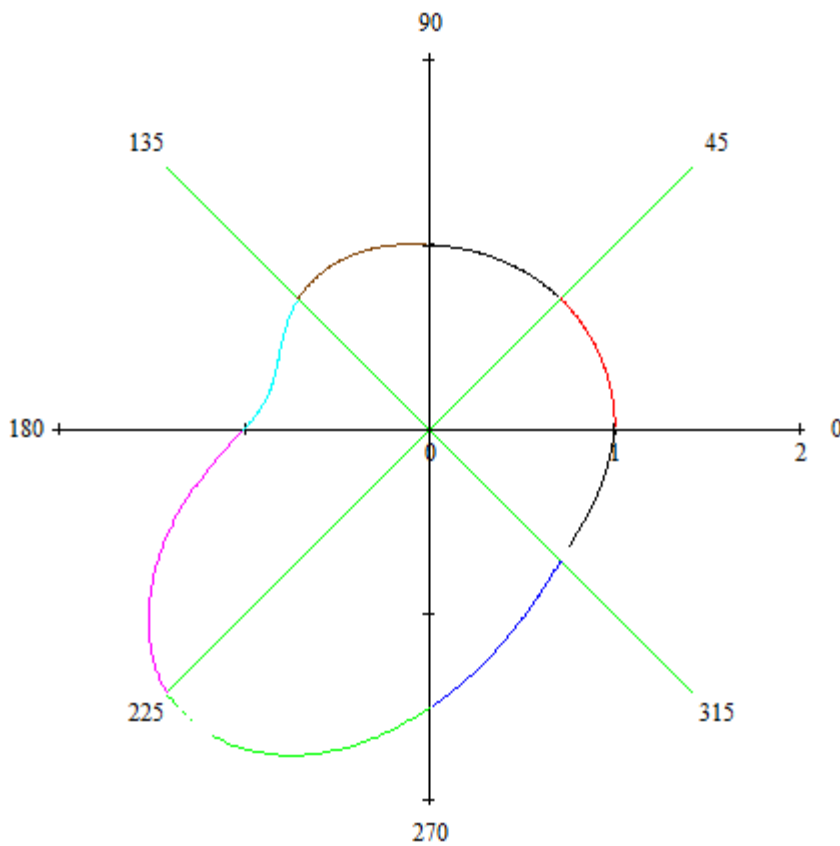


Figure 2: Cubic spline interpolation representation

Geometry optimization technique: Nelder-Mead simplex

The inverse problem requires an iterative method that aids in the search for the subsurface cavity geometry by minimizing the least squares functional comparing the second order (Neumann) boundary conditions. Since the forward problem is computationally expensive for complete grid reconstruction, the Nelder-Mead simplex method is ideal due to minimal forward problem calculations per iteration. The first step in any optimization technique is to define how the unknown parameters are altered to minimize the function/problem being analyzed. The simplex method is defined by the number of unknown parameters that are of interest. The “simplex” is a geometrical figure with $N + 1$ points and N dimensions, where ‘ N ’ is the number of parameters. For example, in a two dimensional problem the simplex is a triangle, and in a three dimensional problem the simplex is a tetrahedron [10]. As for the solution marching logic, the simplex can be manipulated by expansion, contraction and reflection. These three tools are utilized to move the solution with the highest residual error around the solutions of low residual error to find a new minimum. In essence, the simplex is moved in a downhill manner until a tolerance between solutions is reached.

The single cavity problem with known internal boundary conditions requires nine initial guesses of eight parameters. These eight parameters define the shape of the internal cavity. The cubic spline creates high resolution without the drawback of unknown parameter increases. Calculation time is thereby reduced, and the simplex optimization becomes more stable. To minimize these unknown parameters a least squares functional is defined by comparing the Neumann boundary conditions at the surface. Equation 13 defines this functional, where $\{r\}$ is the array containing all of the spline lengths of the AGP, q_c and q_m are the BEM calculated and

IR measured flux of each boundary element respectively, N_{sc} is the scale factor and N_e is the number of boundary elements at the surface.

$$LSF(\{r\}) = \sum_{i=1}^{N_e} \frac{1}{N_{sc}} (q_c - q_m)_i^2 + \alpha(r) \quad (13)$$

$$LSF(\{r\}, \{T_{cav}\}) = \sum_{i=1}^{N_e} \frac{1}{N_{sc}} (q_c - q_m)_i^2 + \alpha(T, q, r) \quad (14)$$

$$\alpha(T, q, r) = \begin{cases} 0 & \text{if } T_{min} < T_{cav} < T_{max} \text{ and } q_{min} < q_{cav} < q_{max} \\ \text{value } O(q, t) & \text{if } r_{cav} < 0 \text{ or } r_{cav} \text{ is outside the system walls} \\ \text{value } O(q, t) & \text{if } T_{cav} < T_{min}, T_{cav} > T_{max}, q_{cav} < q_{min} \text{ and } q_{cav} > q_{max} \end{cases} \quad (15)$$

T_{cav} and q_{cav} are the temperature and heat flux boundary conditions at the cavity walls respectively. The $\{T_{cav}\}$ array defines the temperatures of each boundary element along the cavity wall. If the boundary conditions of the cavity are also part of the unknown parameters, shown by equation 14, the optimization method becomes unstable without the use of the ‘ α ’ function, equation 15. This ‘ α ’ function requires the simplex method to confine its search within the limits that have been setup using educated guesses. In most cases, when there is no heat generation, the temperature within the medium should not reach temperatures higher or lower than that of the surface. Since the cavity is located within the medium, and is most likely filled with a material of much lower thermal conductivity, the heat flux values at this surface are very low relative to the heat flux within the medium. Educated guesses for the maximum and minimum heat flux values are chosen using these principles. Once these limits are exceeded, a value on the order of the temperature and flux calculations is added to the least squares function (LSF). This addition keeps the simplex optimizer away from those unstable values.

Logic behind choosing the initial $N + 1$ guesses is also addressed during the optimization technique. The user provides one educated initial guess for the geometric solution to the

problem. The optimizer then chooses the remaining initial guesses by scaling the geometry, and randomly adding mutations to the scale. The cavity geometry must fit within the medium, so a method for checking geometry stability is proposed. Points along the cavity wall must be contained within the medium, so it can be said that the angles made between each boundary element along the exposed surface will add to 2π . If the point lies outside the medium, this summation becomes zero. Figure 3 shows how these angles add up to 2π when the point is located within the medium and zero when the point is located beyond the medium.

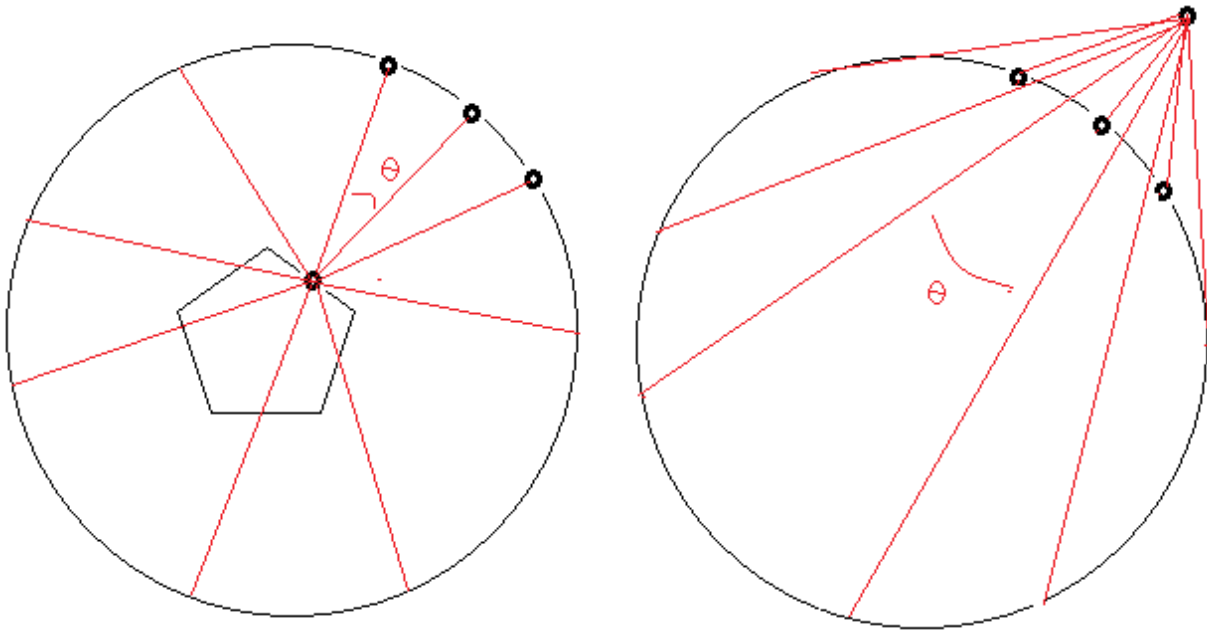


Figure 3: Left - graphical representation of logic employed to keep AGP points within medium. Right - point located beyond the medium.

To calculate these angles appropriately, the connections between the points of the exposed surface and cavity walls are treated as vectors. Simple vector algebra states that the angle between any two rays can be expressed by equation 16.

$$\cos(\theta_i) = \frac{r_{i+1} \cdot r_i}{|r_{i+1}| |r_i|} \quad (16)$$

From equation 16, r_i and r_{i+1} are the successive vectors shown in Figure 3.

The convergence criteria of the simplex method consists of parameter comparison, and LSF residuals. As the simplex marches downhill, the $N + 1$ parameter sets begin to converge to a single set. Once the changes between each set reaches a tolerance set by the user, the optimization stops, and the solution is analyzed. If the solution did not yield a low residual between the Neumann conditions, the weighting parameters for the contraction, expansion, and reflection tools are tweaked. Once the residual condition is satisfied, the solution to the inverse geometry problem is found.

Multiple boundary condition sets (MBCS) can also be used to increase the resolution of the exposed surface without having to add more boundary element locations to the geometry. In a simple example, two boundary condition sets are used as shown in Figure 4. Two identical geometries are imposed with separate boundary conditions to increase the number of boundary conditions being minimized. Essentially two sets of boundary conditions are used to solve one inverse geometric problem. The new LSF looks quite similar to equation 13 with the exception of a second set of boundary conditions. Equation 17 defines the MBCS minimization functional.

$$LSF(\{r\}) = \left(\sum_{i=1}^{Ne} \frac{1}{Nsc} (q_c - q_m)_i^2 \right)_{SET\ 1} + \left(\sum_{i=1}^{Ne} \frac{1}{Nsc} (q_c - q_m)_i^2 \right)_{SET\ 2} \quad (17)$$

This technique is not restricted to two sets, and can be extended further with the implication of speed loss due to increased calculation times. Each set requires an additional forward problem solution per iteration.

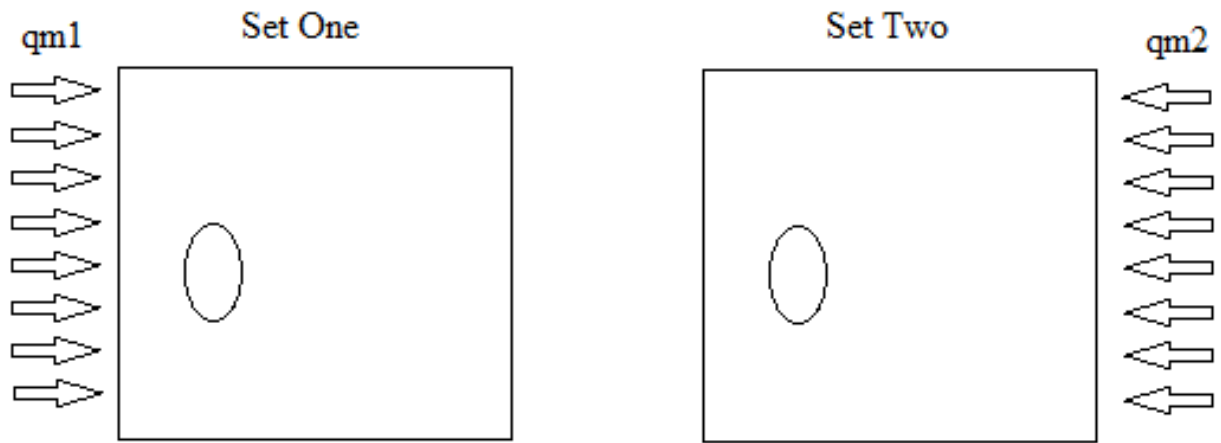


Figure 4: Multiple boundary conditions sets experiment

NUMERICAL EXAMPLES

Case 1: Boundary element method testing

The geometry being tested is a hexagon with two interior holes. The geometry is split into 16 constant elements, and a BEM solver is used to compute the heat flux at the boundaries as a result of forced temperature boundary conditions. See Figure 5 for this test geometry.

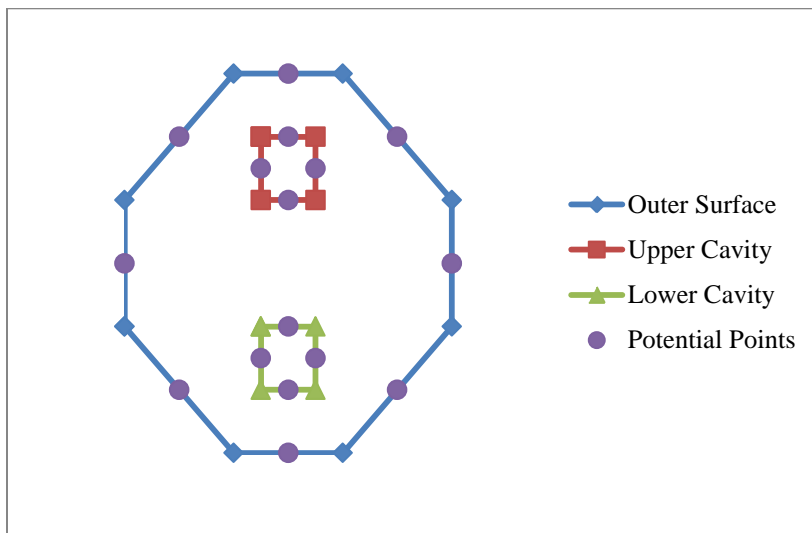


Figure 5: Case 1 geometry of hexagon with two cavities

To verify the BEM results, the calculated heat flux is compared to the actual imposed heat flux at each point along the boundary. The error in these calculations is due to the low resolution of the boundary elements. These comparisons are shown in Figure 6. As the figure shows, the difference between the calculated and imposed conditions are minimal, which proves that the BEM being used has successfully calculated the temperature field and boundary conditions. Higher resolution elements can be used to minimize the error, which is demonstrated in Case 2.

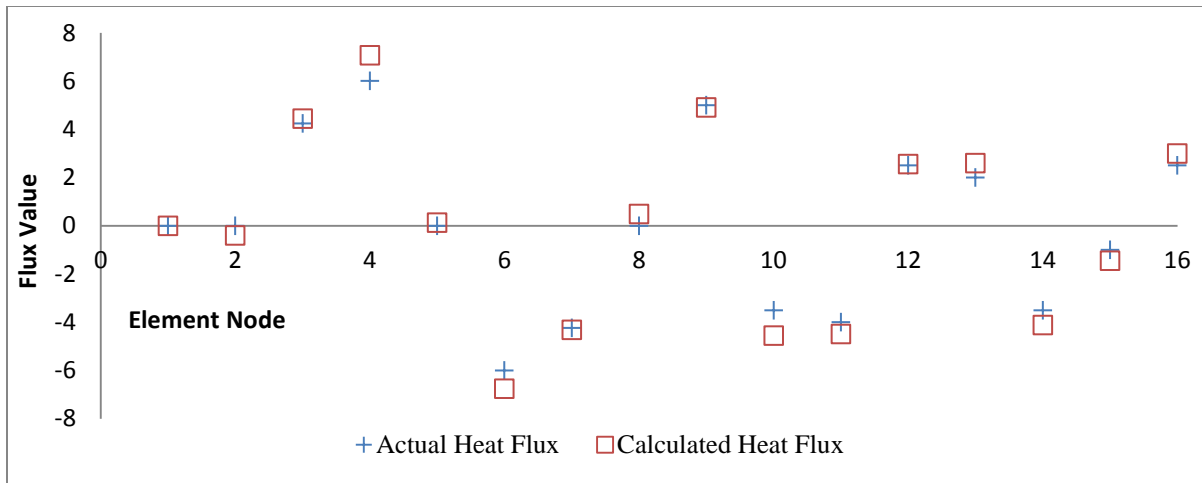


Figure 6: Case 1 analysis of error in flux calculations using BEM

Case 2: Source and high resolution testing

The geometry being tested is a solid annulus with 64 boundary elements. This high resolution is chosen to decrease the error that was encountered in the previous BEM testing in Case 1. This case also includes sources within the medium of the annulus. Figure 7 depicts the annulus geometry along with source locations within the medium.

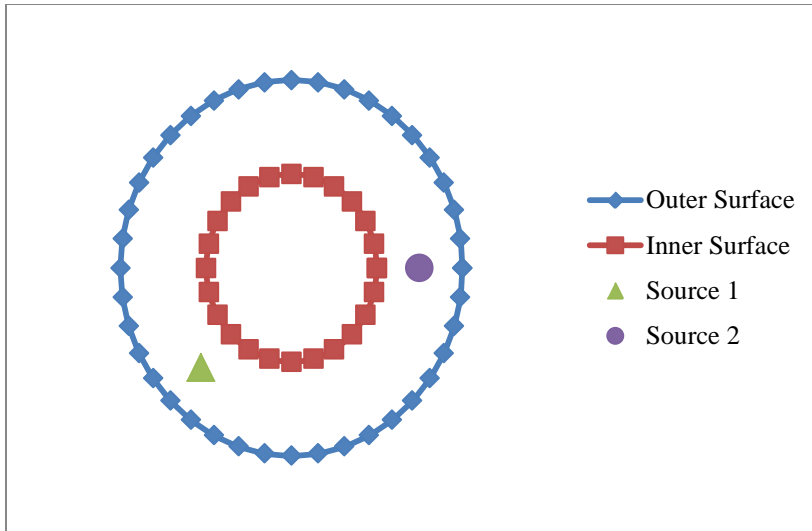


Figure 7: Case 2 geometry of annulus with source locations

The main purpose of this test is to confirm the BEM calculations involving point source locations within the medium. It is also interesting to see the decrease in calculation error when using higher resolution boundary elements. As Figure 8 shows, the error between the imposed and calculated flux boundary conditions is nearly non-existent.

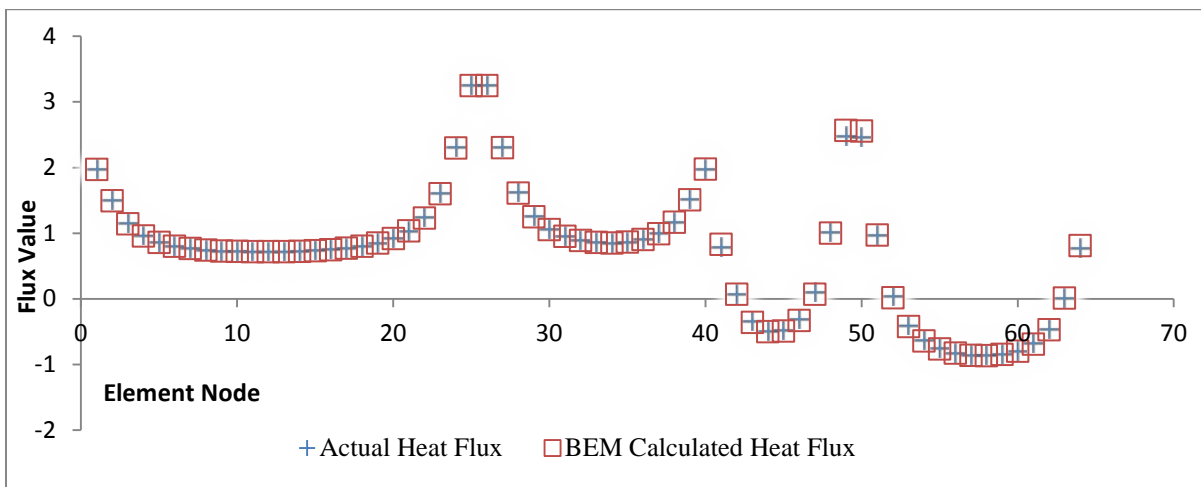


Figure 8: Case 2 analysis of error in flux calculations using BEM

Case 3: Cavity detection testing

The cavity location is found by introducing a source into the medium, and optimizing the heat flux output of the measureable surfaces. In this example the outer surface and inner surface geometries are known and measurable. The cavity is then found by using a Nelder-Mead simplex method to optimize the location and strength of the test source. The following four figures (Figure 9, Figure 10, Figure 11 and Figure 12) depict the iterative steps taken to find the cavity.

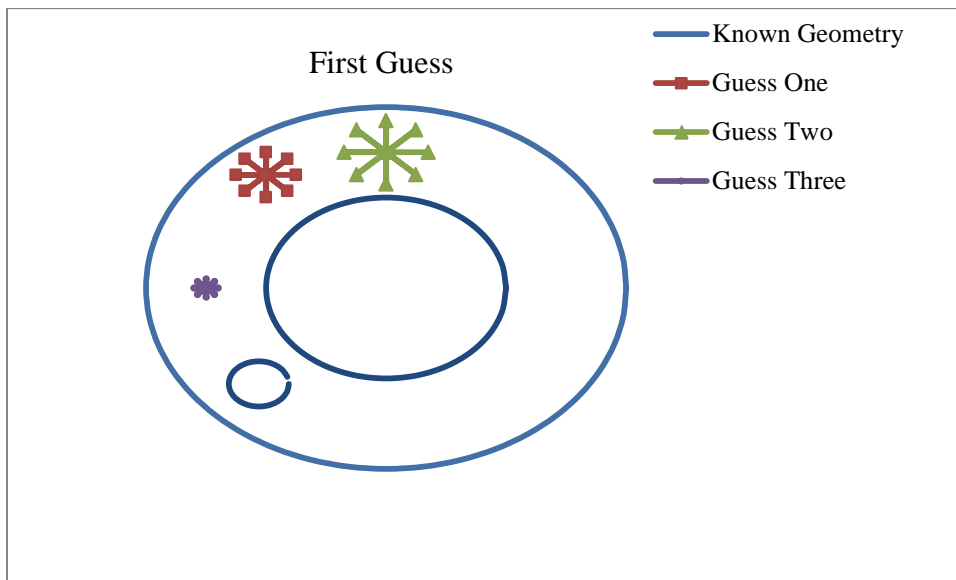


Figure 9: Case 3 first guess source locations

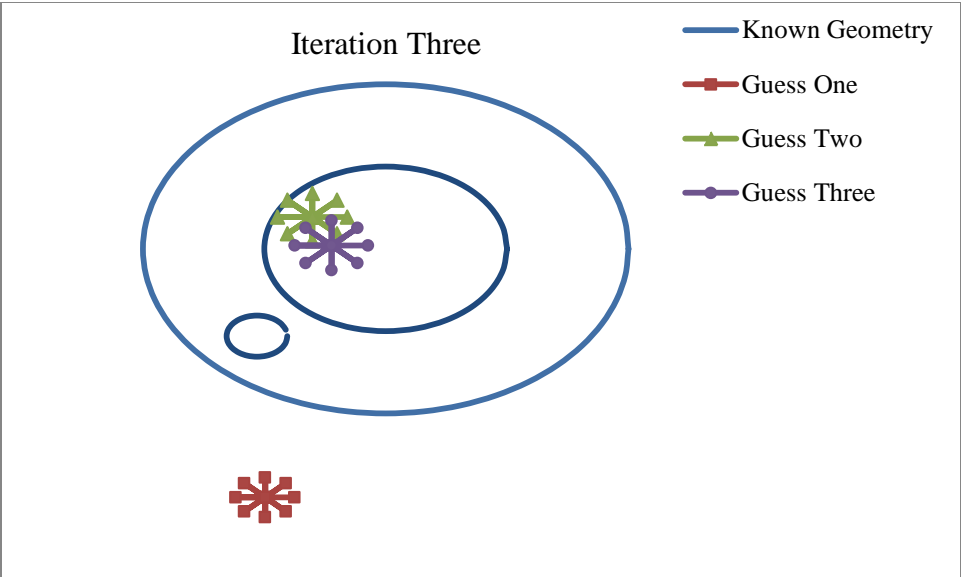


Figure 10: Case 3 third iteration source locations

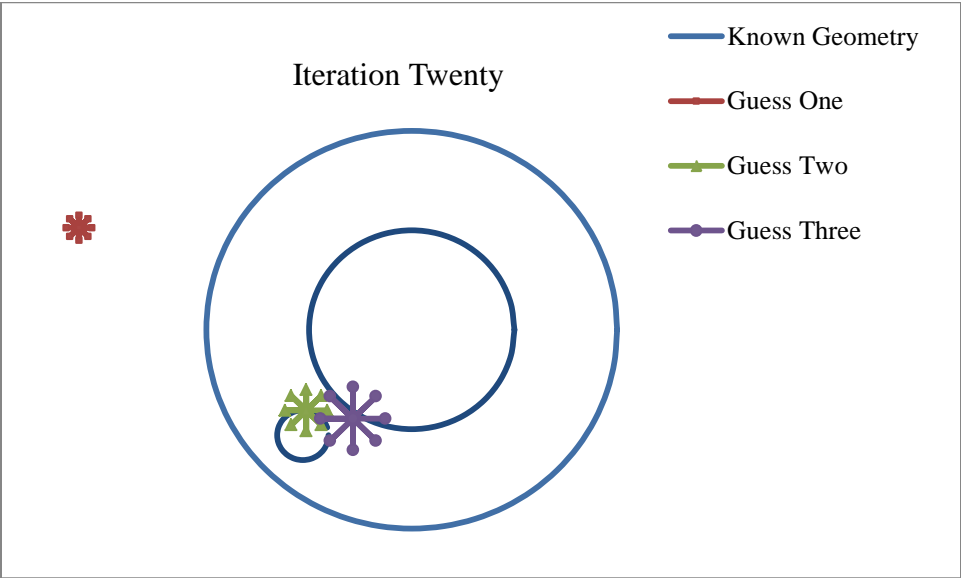


Figure 11: Case 3 twentieth iteration source locations

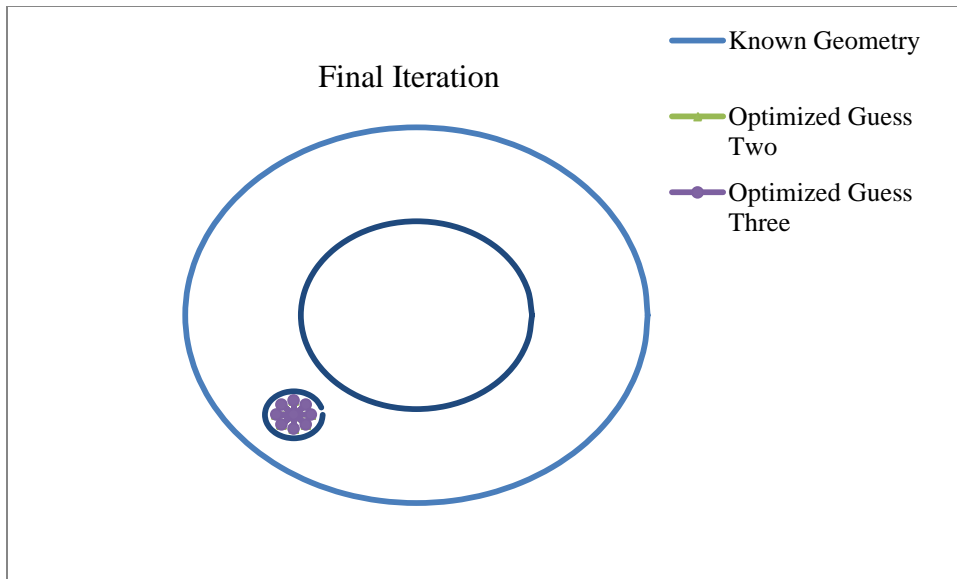


Figure 12: Case 3 final solution source locations

In Figure 10, the first cluster of sources is thrown away from the geometry, and the second and third clusters begin to move toward the cavity. Figure 11 depicts the same movements as Figure 10. The first cluster is moving farther away, whereas the other two are moving toward the cavity. The last figure, Figure 12, verifies that the clusters have found their way into the cavity, and the first cluster has gotten so far away it no longer affects the solution. It should also be noted that by observing the calculated temperature and heat flow magnitude contour plots, Figure 13 and Figure 14, the cavity location can be determined.

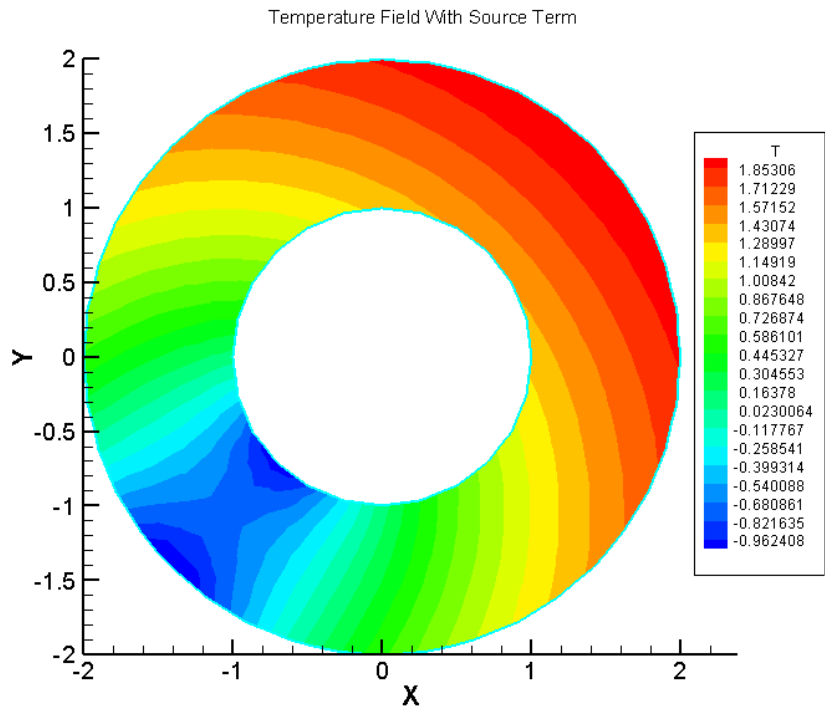


Figure 13: Case 3 temperature field with source term of final solution

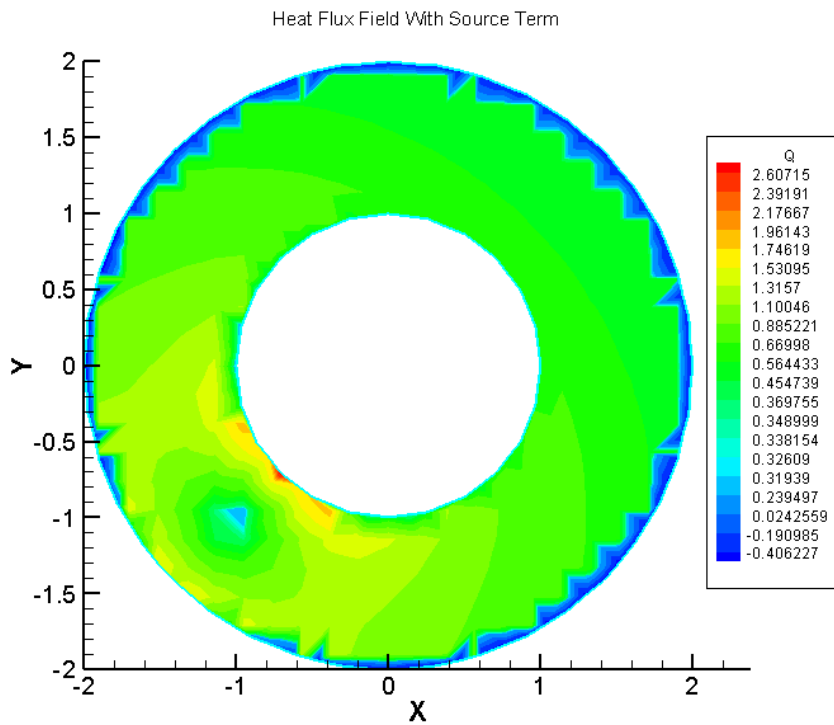


Figure 14: Case 3 heat flow magnitude with source term of final solution

Case 4: Geometry reconstruction testing

Once the center of the cavity is found using point source techniques, the surface of the cavity is generated. The cavity surface is created by guessing radial values of an anchored grid pattern using a periodic cubic spline interpolation. Points along the cubic spline are then selected and segmented into BEM surface elements. In this particular example, 32 elements have been created. The forward problem can now be solved using the anchored grid pattern as the interior cavity. The cavity geometrical parameters are then optimized using a Simplex method. Figure 15, Figure 16 and Figure 17 depict the iterative process

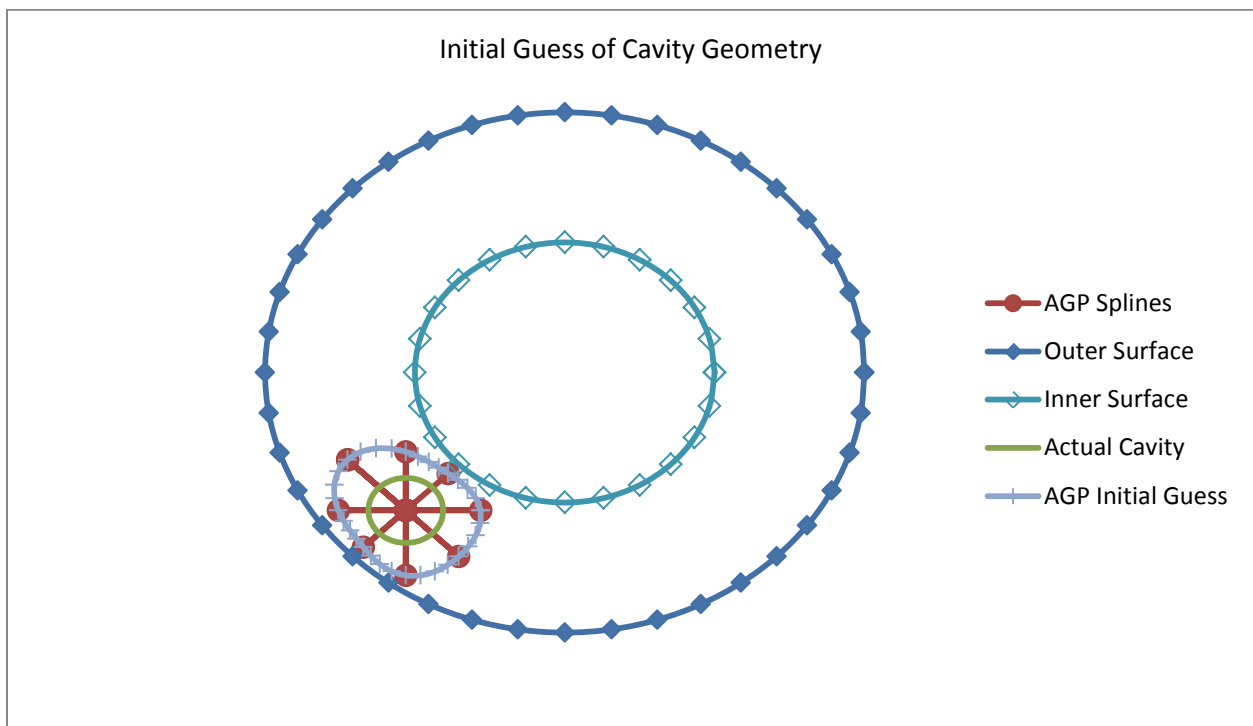


Figure 15: Case 4 initial guess of cavity geometry

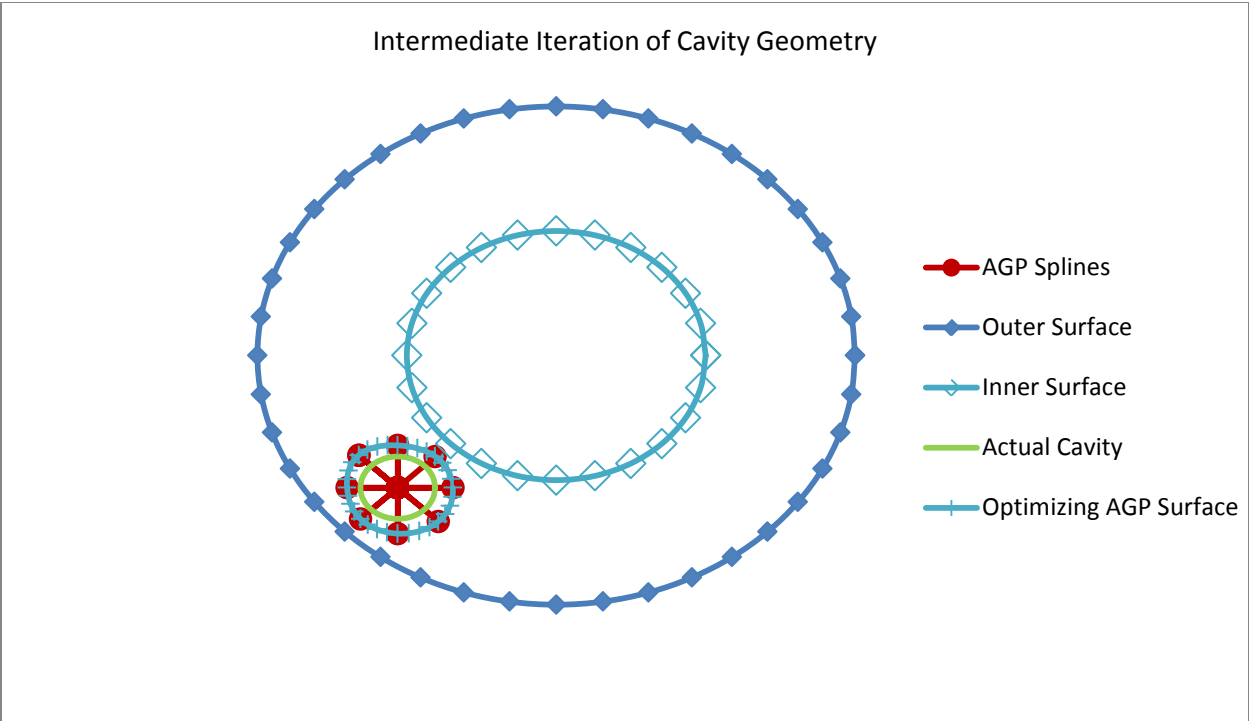


Figure 16: Case 4 intermediate iteration of cavity geometry

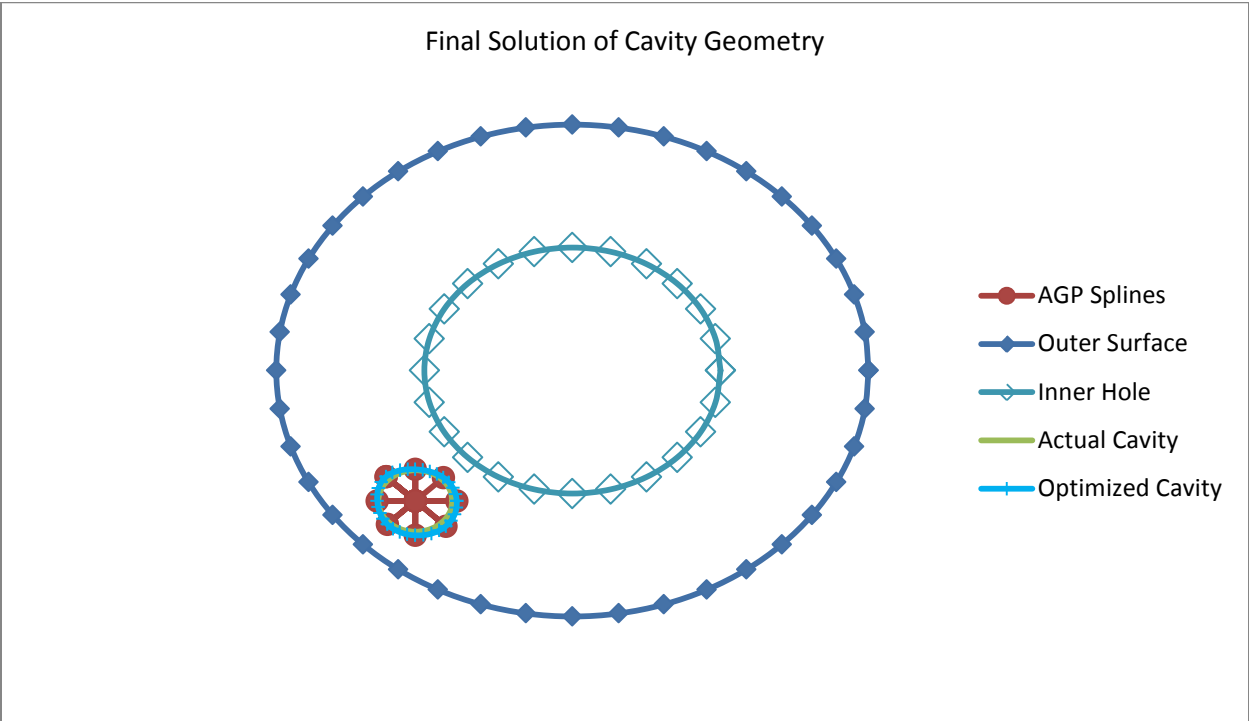


Figure 17: Case 4 final solution of cavity geometry

In Figure 15, the initial guess for the geometry is much larger than the actual cavity. The splines in each figure were used to calculate the geometry surface using the cubic spline interpolation explained above. Figure 16 is one of the intermediate steps taken to optimize the cavity geometry. The solution is then verified in Figure 17.

Case 5: Single cavity reconstruction experiment

This next experiment involved realistic boundary conditions of both temperature and heat flux values. An irregular shaped cavity was imposed with a very low constant heat flux at the surface. The outer boundary is insulated on the top and bottom walls, whereas the temperature is imposed at the left and right surfaces of the outer boundary. As in the previous example, the hole is found using point source techniques. Once the location is found, the surface generator takes over and optimizes the cavity geometry. The optimizer is initialized with two initial guesses as shown in Figure 18. The AGP splines are then used to generate the cavity surface and section into boundary elements.

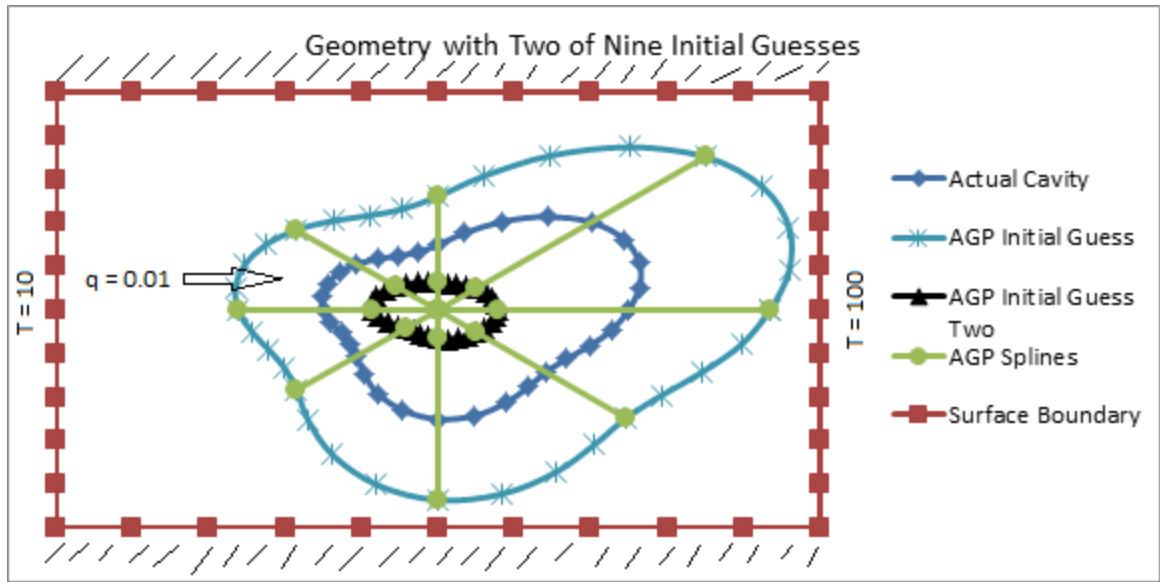


Figure 18: Case 5 geometry and initial guess locations

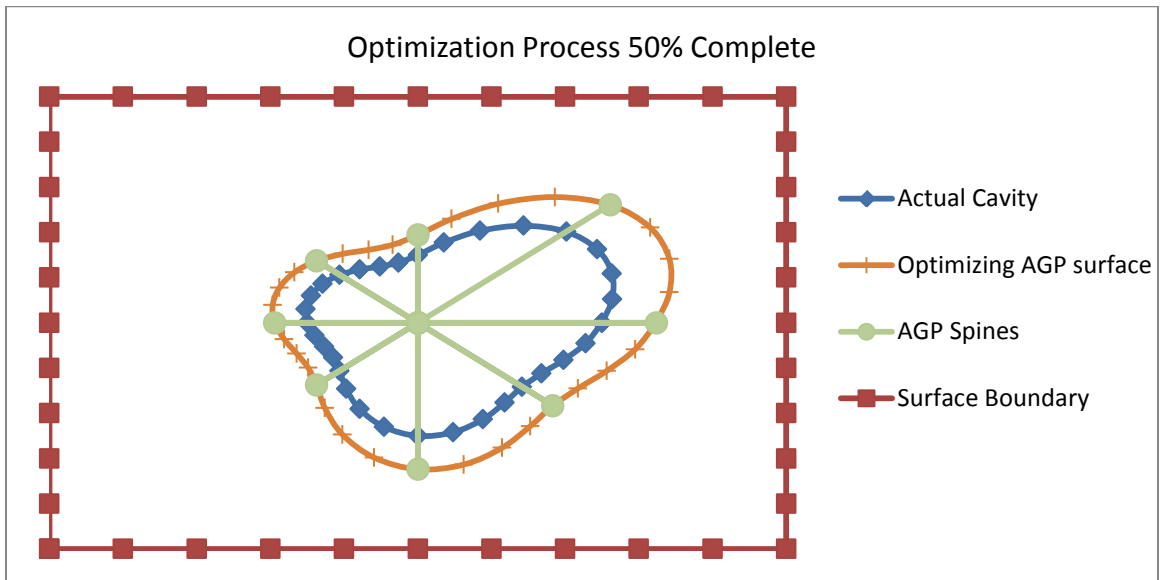


Figure 19: Case 5 optimization process 50% complete

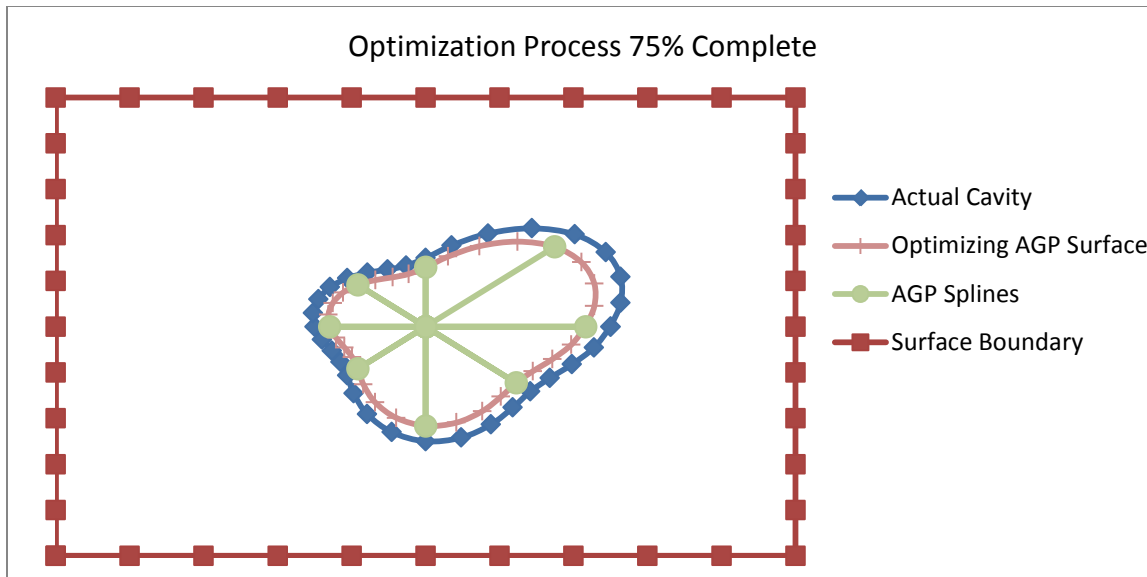


Figure 20: Case 5 optimization process 75% complete

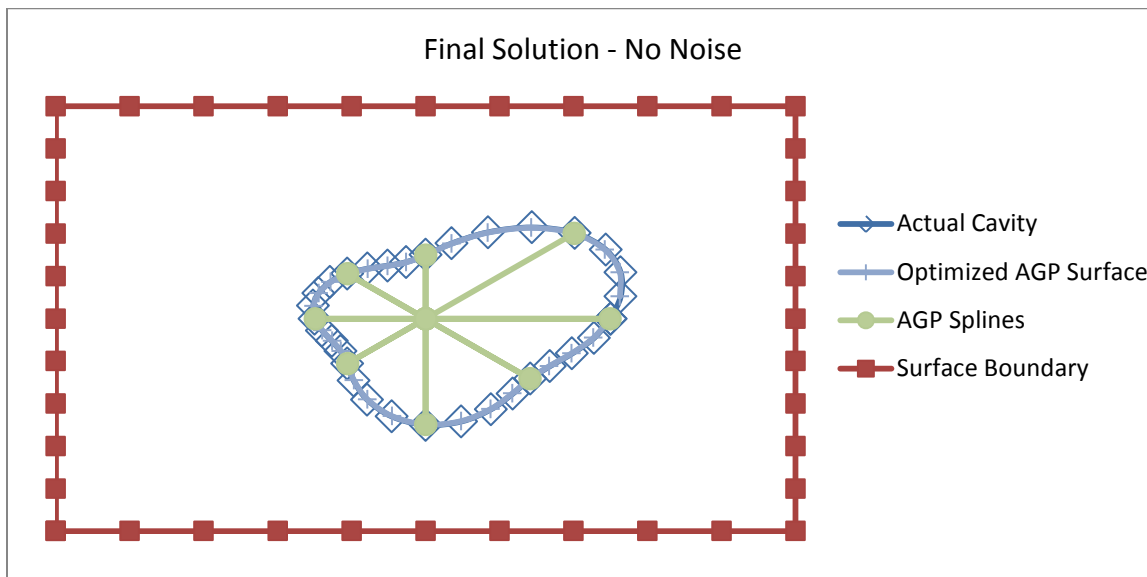


Figure 21: Case 5 final solution, no noise in measurements

After several iterations, the unknown cavity surface was found. Figure 19 and Figure 20 depict the intermediate steps taken to arrive at the optimized solution. The final solution is shown in Figure 21, which is observed to have high accuracy. While the BEM is optimizing the

geometry based on surface heat flow measurements, it is also minimizing the temperature and heat flux contours. Figure 22 and Figure 23 show the difference between the initial guess and final solution temperature contours. The same can be said about the heat flux magnitude contours in both the initial guess and final solution heat maps in Figure 24 and Figure 25.

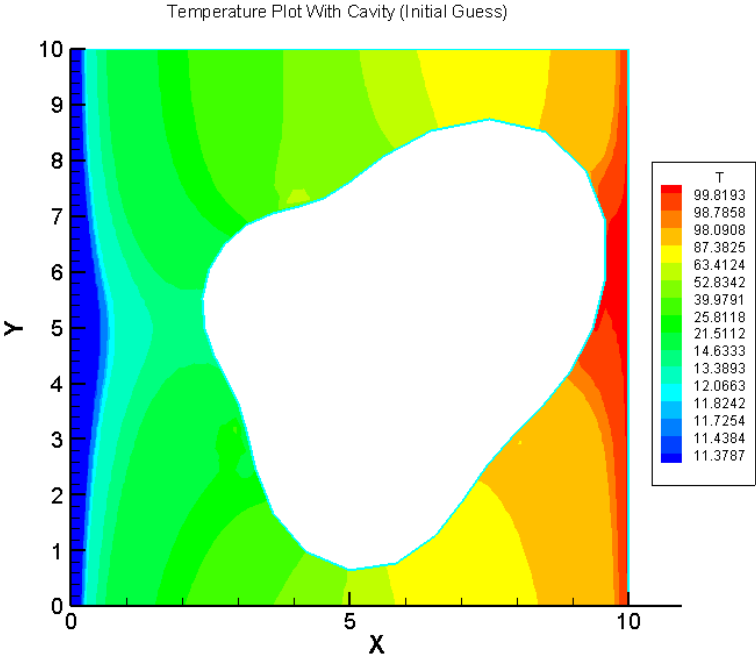


Figure 22: Case 5 initial guess temperature plot

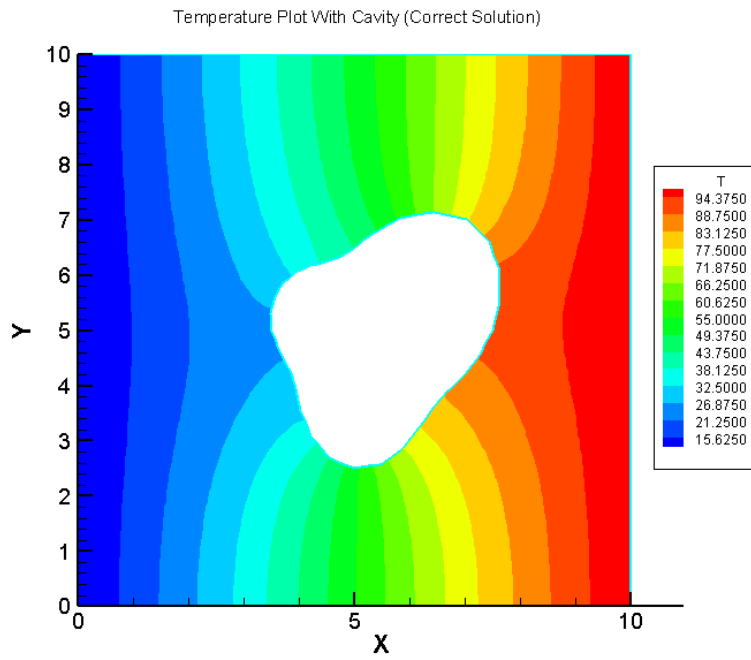


Figure 23: Case 5 final solution temperature plot

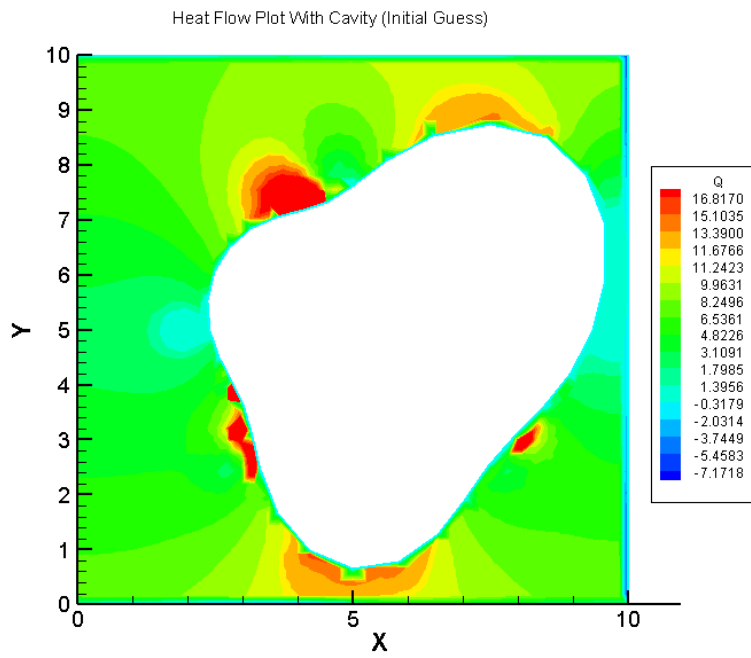


Figure 24: Case 5 initial guess heat flow magnitude plot

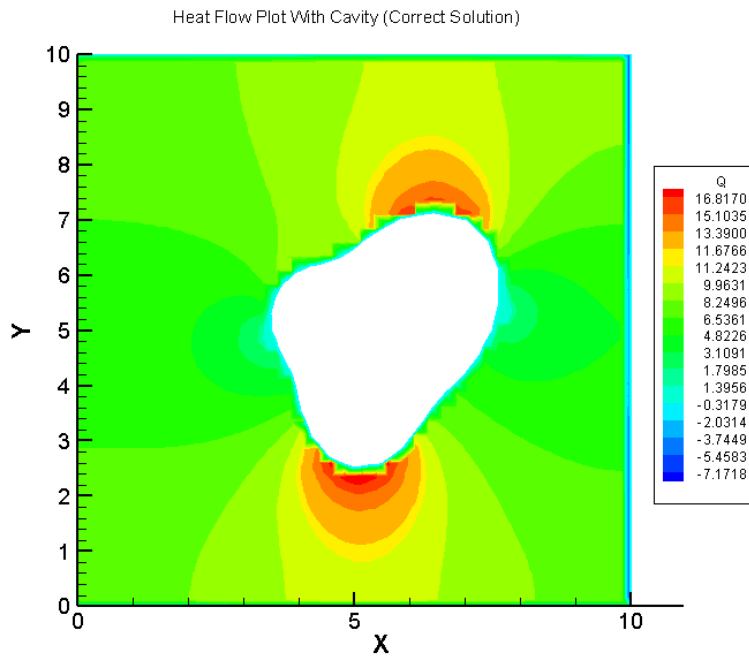


Figure 25: Case 5 final solution heat flow magnitude plot

Case 6: Single cavity reconstruction with noisy measurements experiment

In practical applications where experiments provide the over-specified conditions required to solve the inverse problem, the exact boundary conditions cannot be measured exactly. To simulate these conditions noise was added to the exact boundary conditions on the exterior surfaces (the boundary conditions that would be measured with instrumentation). Three separate experiments were carried out to observe the behavior of resultant cavity geometry based on noisy measurements. First, one percent error was added to the flux boundary conditions and the final solution is shown in Figure 26. It is observed that there are some deviations from the correct cavity geometry, which are incurred by the noisy data.

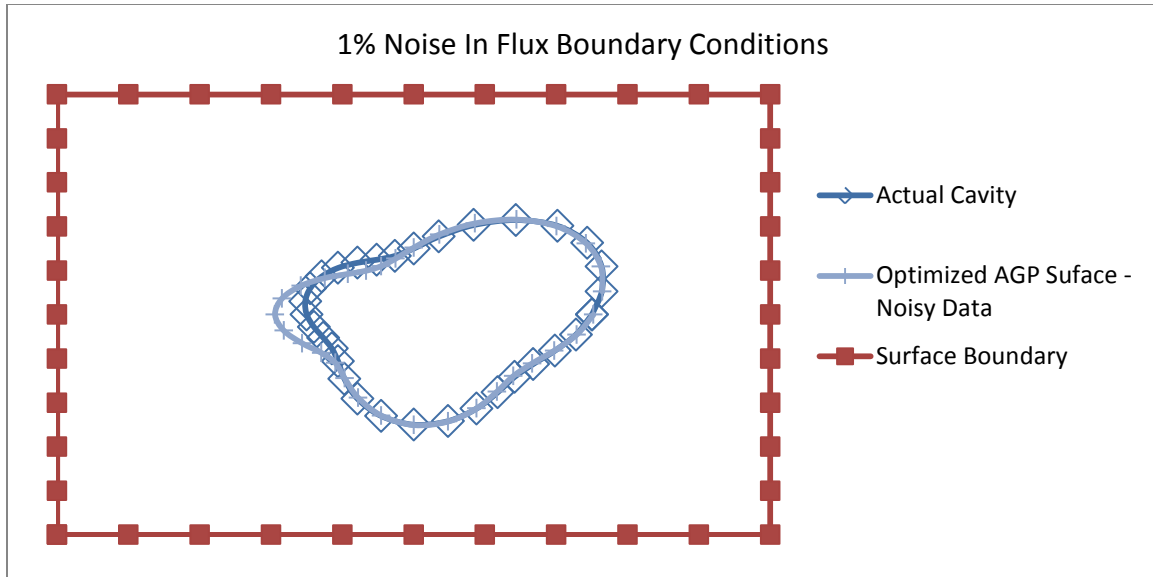


Figure 26: Case 6 with 1% noise in flux boundary conditions

Second, a two percent error was added to the flux boundary conditions. Similar results were found and shown in Figure 27. As expected, the larger error measurements lead to larger deviations in the cavity geometry being optimized. It is also interesting to note that the largest deviations occur in the parts farthest from the surface. As the cavity size reduces, or gets farther from the outer boundary, it becomes more difficult to detect due to its low effect on the heat signature. This is the motivation for the use of multiple boundary conditions to increase the resolution of the inverse problem algorithm as will be demonstrated in the last section of this chapter.

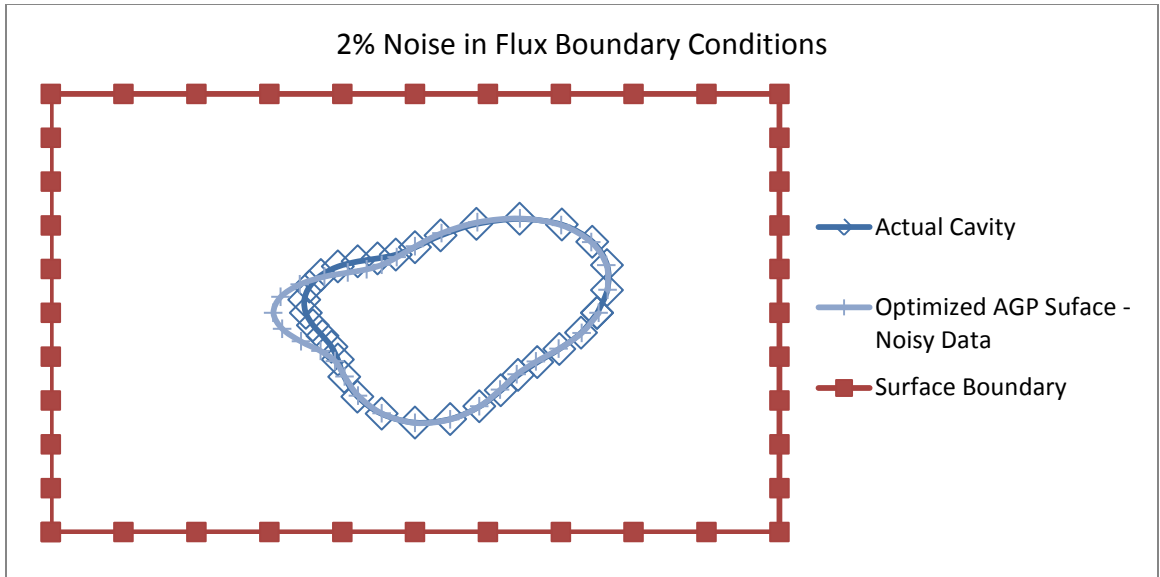


Figure 27: Case 6 with 2% noise in flux boundary conditions

The last noise experiment involved one percent error in both the temperature and flux readings. The BEM optimizer successfully approximates the cavity geometry with small error as Figure 28 implies.

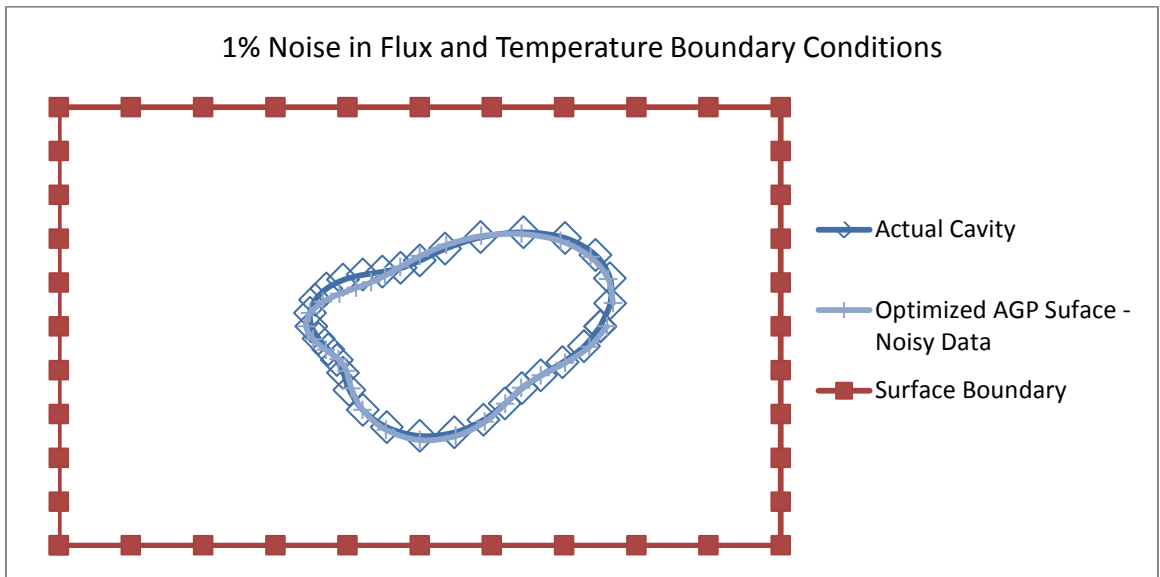


Figure 28: Case 6 with 1% noise in both the temperature and flux boundary conditions

Case 7: Multiple cavity reconstruction experiment

Multiple cavities can also be discovered using the same principles previously discussed, but with multiple cavity surface generators. In this experiment, two cavities were placed inside an arbitrarily shaped object, as shown in Figure 29. Boundary conditions were then applied, and the remaining boundary conditions were found using BEM. The interior boundary conditions can also be unknown. Rather than assuming the cavities to be insulated and known, the boundary conditions can also be found by adding them as parameters to the simplex optimizer. The boundary conditions must be restricted to reasonable values to reach a stable solution.

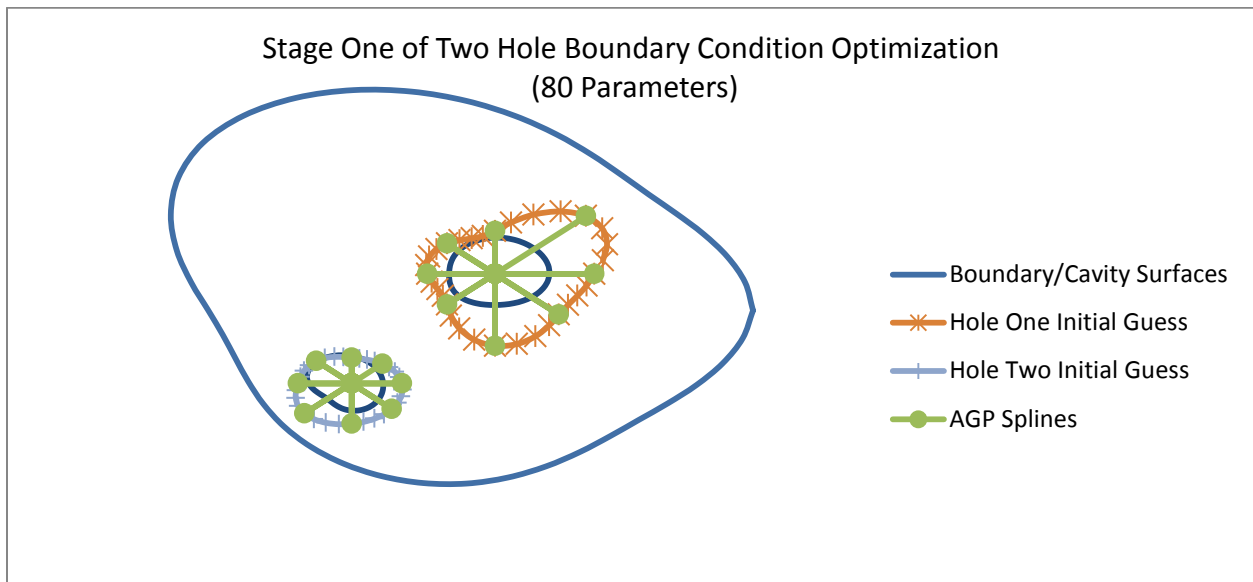


Figure 29: Case 7 initial guess of two cavity 80 parameter optimization

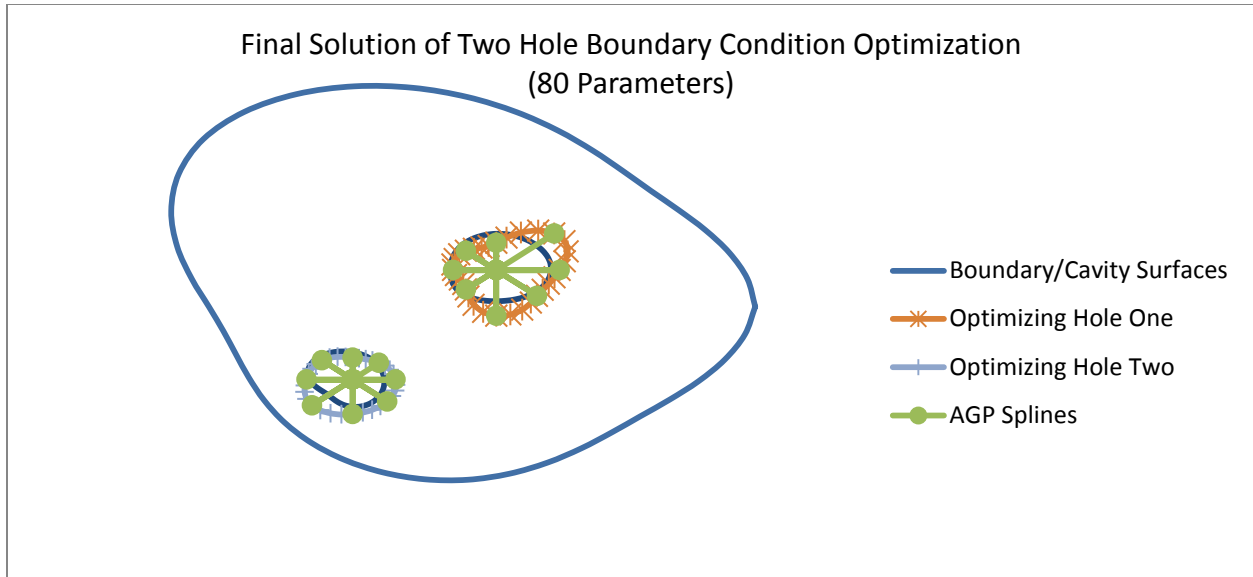


Figure 30: Case 7 final solution of 80 parameter optimization

It is observed that the exact solution to this multiple cavity problem has not been found. A local minimum was found using the simplex method; however, as depicted in the Figure 30, this solution was not expected. Different methods for moving toward a global minimum are needed for multiple cavity problems that involve boundary condition optimization. A genetic algorithm should be applied to solve this local minimum issue. This error is a result of the large number of parameters being optimized in the two cavity case. In this particular example, there are 80 parameters being optimized: 16 for the geometry, and 64 for the boundary conditions.

Since the internal cavities do not provide much conductivity, the heat flow through the cavity can be closely approximated to zero. The 80 parameter problem has now been reduced to 16 geometrical parameters, and the simplex method runs much smoother to find the global minimum. The problem being solved is shown in Figure 31. These particular boundary conditions are chosen to create a temperature field that will show large differentiations on the

boundaries due to interior cavities. The internal cavities are found using the simplex method and are shown in Figure 32. The calculated cavities are a close match to the test geometry that was set up as an experiment, but there are some deviations due to the approximations incurred from constant element BEM. Creating a higher resolution geometry would help to remove some of this error. Figure 33 shows steady convergence of the two cavity problem. The convergence criterion for this case was set to $10E-06$. The final solution was found in 623 iterations using the Simplex method.

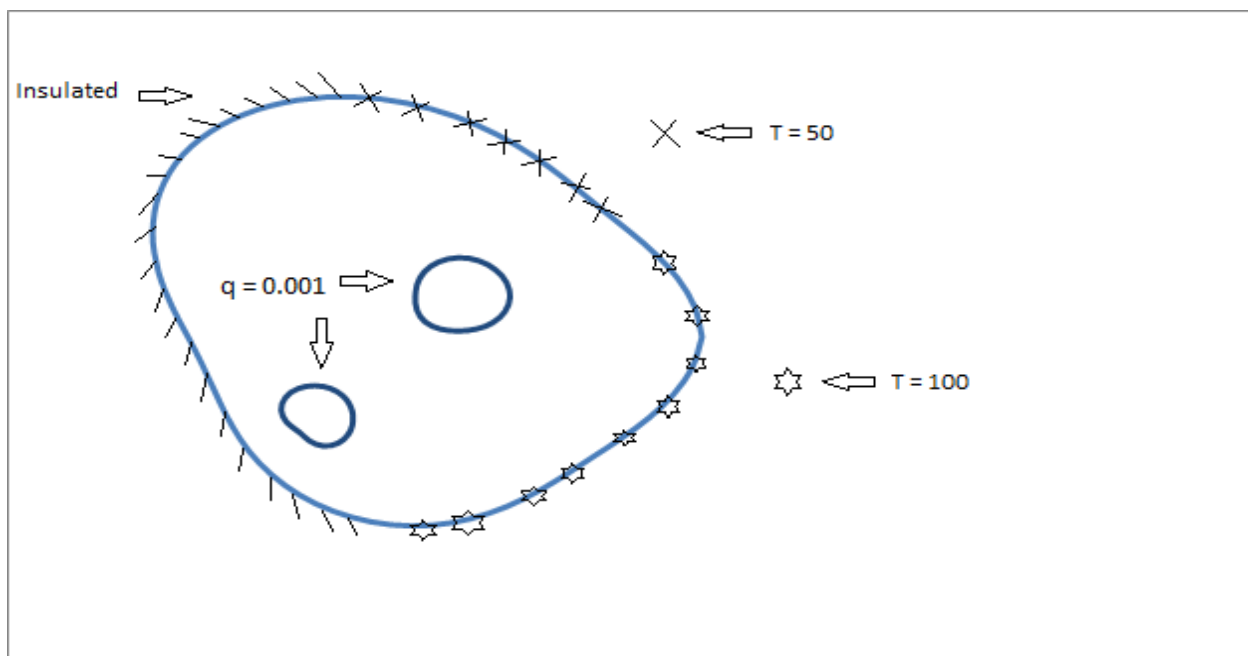


Figure 31: Case 7 geometry and boundary conditions

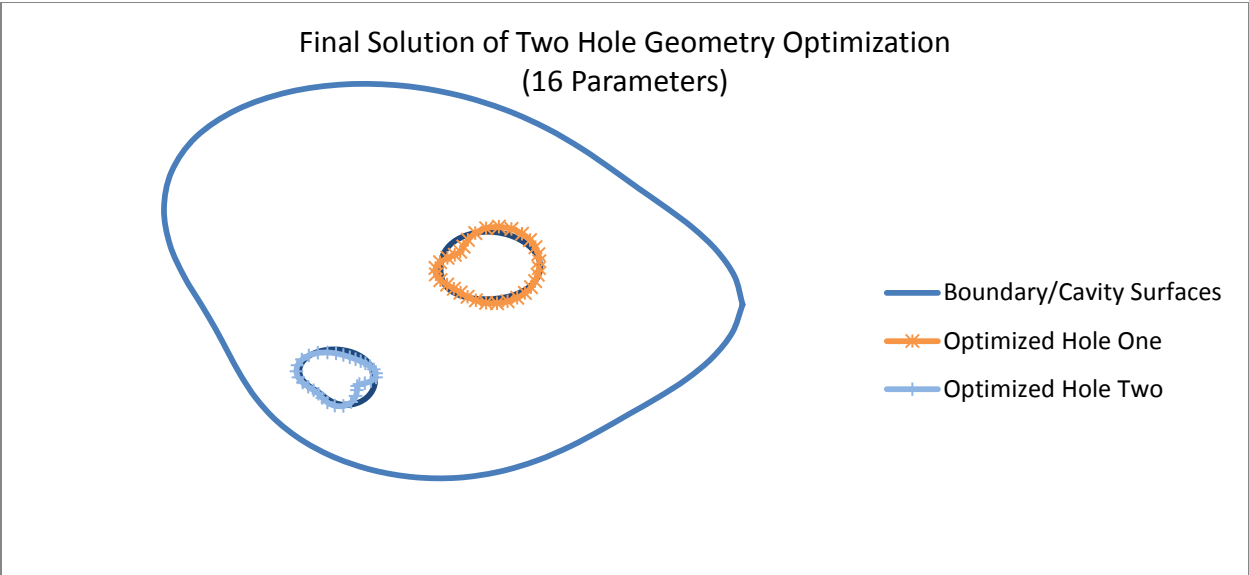


Figure 32: Case 7 final solution of 16 parameter optimization

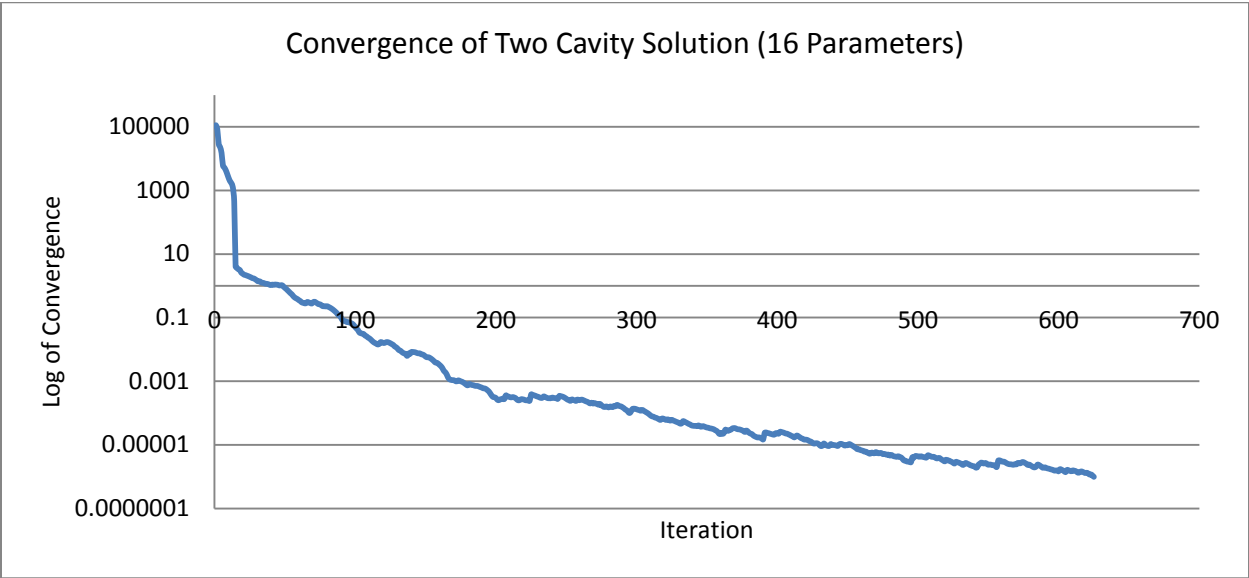


Figure 33: Case 7 convergence plot of 16 parameter optimization

Case 8: Notch cavity reconstruction experiment

Cavity geometries with non-circular shapes are also of interest when detecting unknown cavities. The star shaped anchored grid pattern (AGP) comes into question when the shape of the cavity has sharp edges, turns or corners. Figure 34 outlines the geometrical setup used to test the star shaped AGP against notch shaped cavities. The block is a 10x10 unit structure with 40 boundary elements along the exposed surface. The exposed surface boundary conditions were chosen to create a temperature field that would be highly affected by the internal notch. The internal cavity is represented by 29 boundary elements with known adiabatic wall conditions.

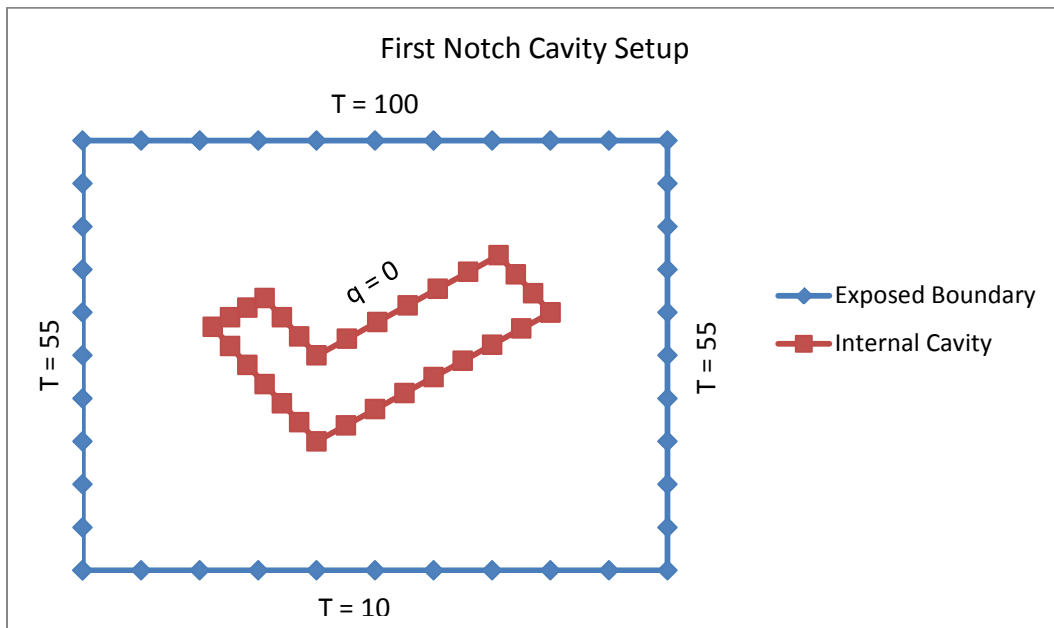


Figure 34: Case 8 experimental setup one

The shape optimization in this case did not accurately predict the shape of the notch. This error is due to the AGP shape itself. As the splines are trying to find their way to the correct solution, they end up crossing the actual cavity walls twice due to the sharp corner of the notch.

The AGP was successful in following the general shape of the notch, especially on the right side of the notch where there is no sharp corner. Figure 35 depicts the calculated cavity over the actual cavity. Star shaped AGP setups are not sufficient in predicting these types of shapes; however, they lend themselves to the idea of differently shaped anchored grid patterns. Antennae shaped patterns are proposed in Kassab et al [3] in their research involving elastostatic geometry optimization, much like the shape depicted in Figure 36.

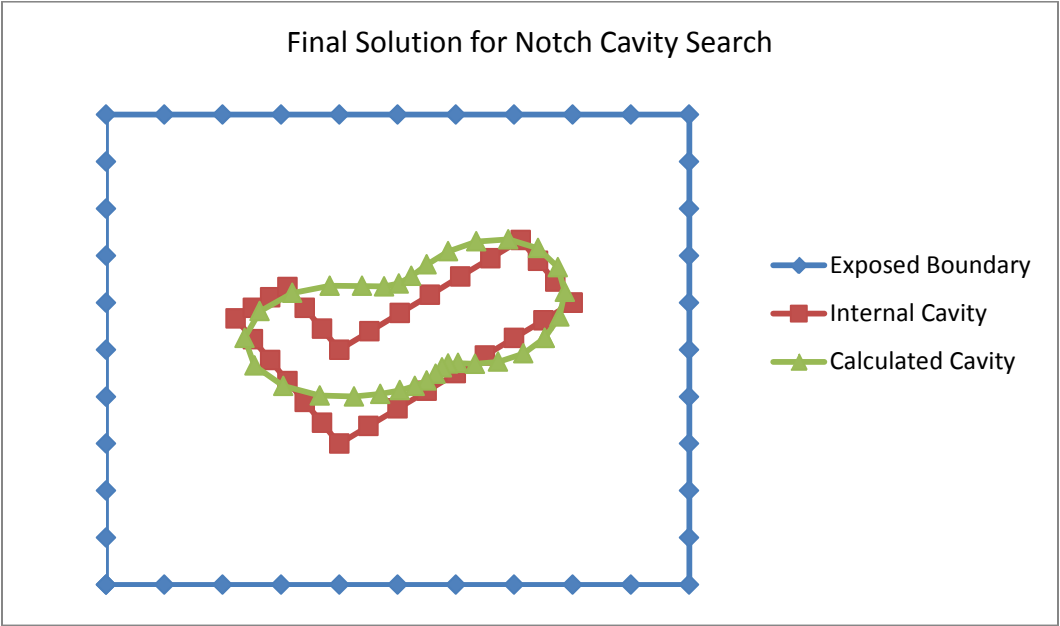


Figure 35: Case 8 final solution to the notch cavity search using one set of boundary conditions

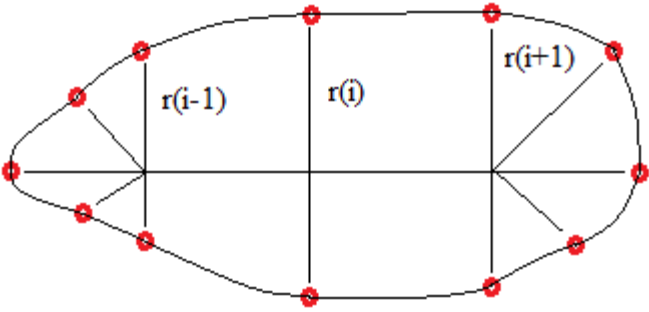


Figure 36: Antennae pattern anchored grid pattern concept

Case 9: Multiple boundary condition set optimization

Multiple boundary condition setups help to alleviate the error incurred by using star shaped anchored grid patterns. As discussed in the ‘solution procedure’ section, multiple boundary condition setups can be used to increase the resolution of the exposed boundary without adding more boundary elements. In case 9, the same notch geometry is used from case 8, as well as the boundary conditions for the first setup, Figure 34. The second boundary condition setup is displayed in Figure 37. The same geometry is used; however, the boundary conditions along the exposed surface have been changed to create a different thermal footprint for the optimizer to minimize.

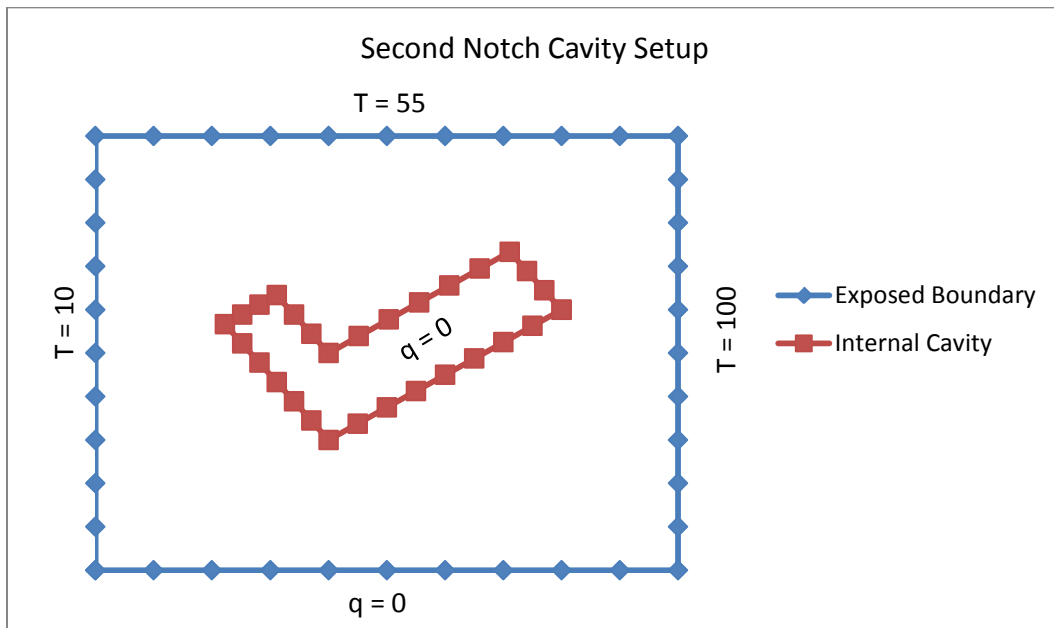


Figure 37: Case 9 experimental setup two

Figure 38 suggests the final solution to the cavity geometry in case 9 is much better than the case 8 solution. The star AGP correctly identifies the right portion of the notch, but it has

severe issues with the corner section of the notch. The interpolator compensates by cutting in and out of the correct geometry, but does not predict the sharp corner of the notch. As stated in case 8, a different AGP design should be implemented when cavities of this shape are encountered. To properly assess the validity of the predicted geometry, the least squares functional can be analyzed by comparing its value to zero and the values being optimized. In this case, those optimized values are the flux conditions at the boundary. In case 8 the values stayed around 5.25, and in case 9 those values dropped to 1.25. For the sake of comparison, the cases that involved successful geometry reconstructions had least square values of 0.01 or less.

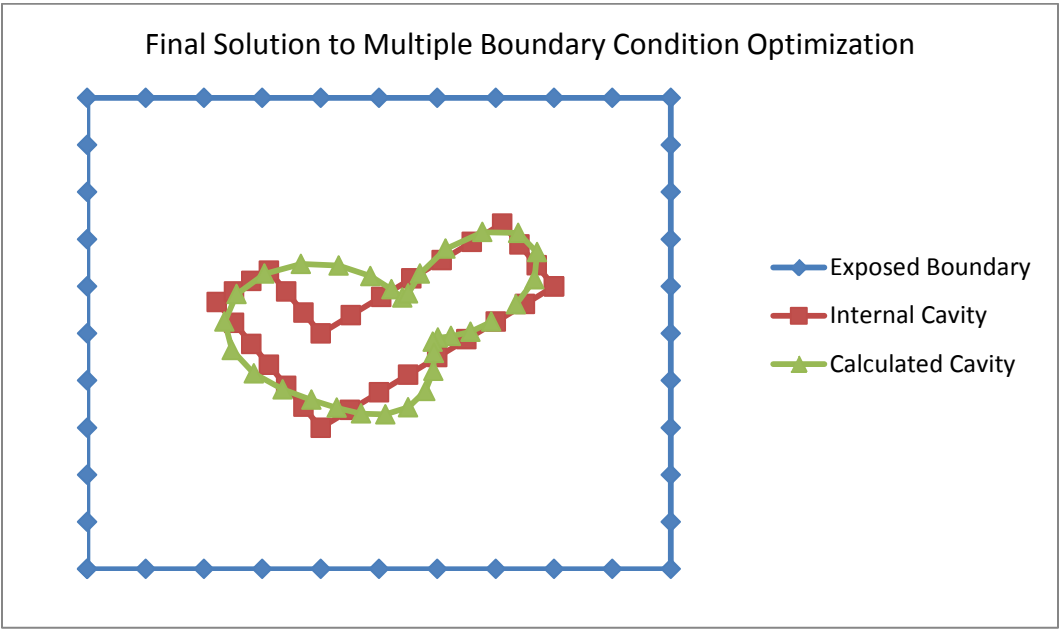


Figure 38: Case 9 final solution to the notch cavity using multiple boundary condition sets when optimizing the cavity parameters

Case 10: MBCS using environmentally realistic boundary conditions

To further prove MBCS optimization techniques a more realistic boundary condition setup is used. Up to this point the boundary conditions that have been applied to the test geometries have been chosen to create distinct heat signatures which are easily detected at the surface.

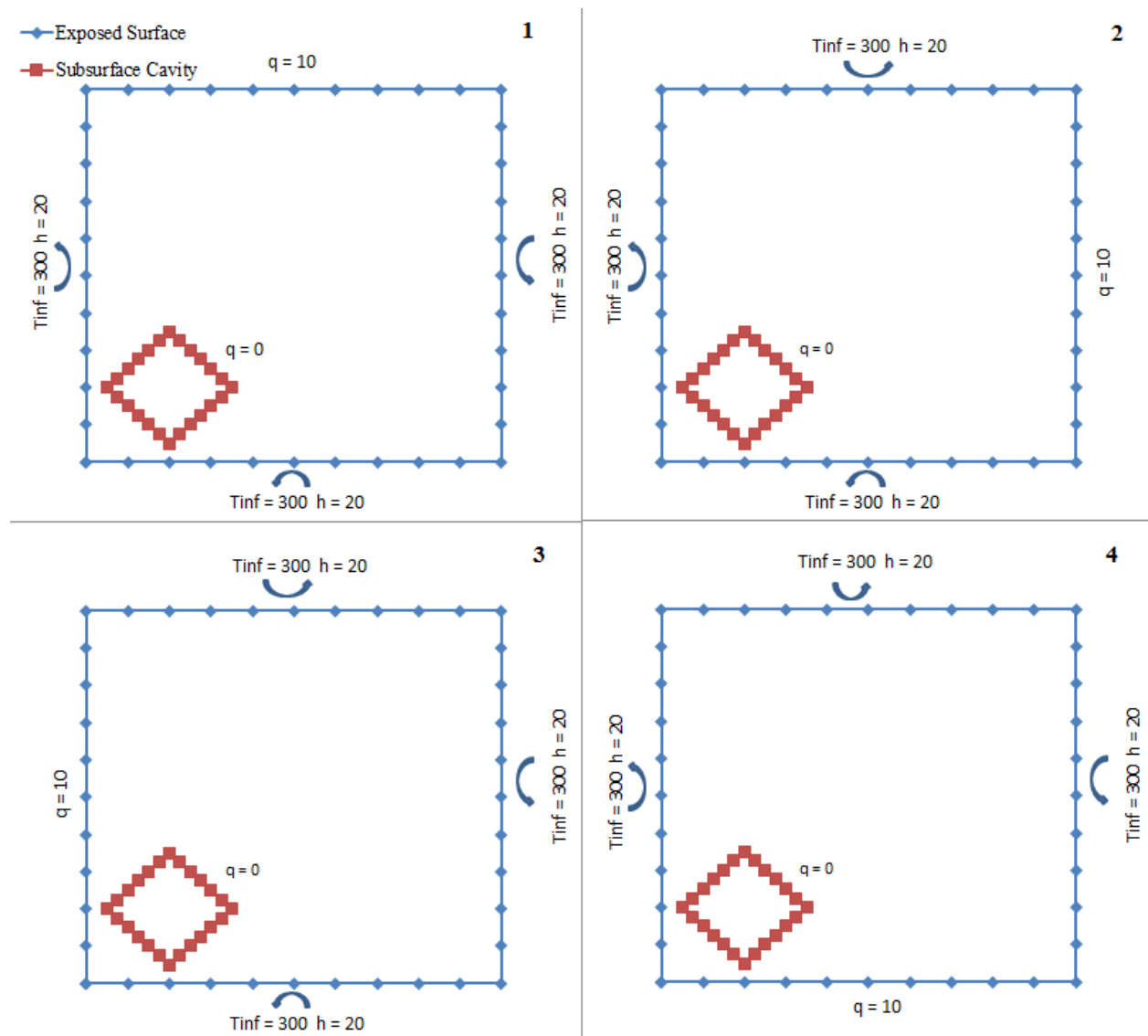


Figure 39: Case 10 boundary condition setup

If the cavity location or shape does not cause significant heat signature differences it may be difficult to locate. Hence, MBCS is proposed to solve this problem, as discussed in Case 9. These techniques can be extended to actual experiments, which would involve convective boundary conditions rather than imposed Cauchy conditions. The experimental setup involves the same 10x10 unit square; however, the cavity has been moved to the corner to limit the sensitivity of the cavity's effect along some of the square's boundaries. Figure 39 displays the four different boundary condition setups that are used in this experiment. In all four setups a heat flux is applied to one side, while the other three sides are subjected to convection conditions at room temperature. Simply put, a heater is placed on one side of the square while the rest of the sides are free to interact convectively with its surroundings. The heater is then moved to the next side and the rest of the sides interact convectively. This procedure increases the sensitivity of the cavities effect on the boundaries, even with difficult cavity locations or poor boundary conditions. First, setup 1 and 2 are used to compute the cavity geometry using MBCS. Figure 40 provides the results from this two boundary set problem. As the results indicate, the cavity geometry is successfully predicted at all edges except for top left side of the diamond. This error is a result of poor boundary condition setup with respect to the location and shape of the cavity. To prove the effectiveness of MBCS beyond two boundary condition sets, setups 1 to 4 are used to calculate the cavity geometry. Figure 41 depicts the four boundary set solution and the result speaks for itself. The cavity geometry is predicted with high accuracy due to increased resolution provided by the four sets of boundary conditions. Separately, each boundary condition set is inefficient in its use for optimization; however, when all four sets are combined the needed information is exceeded.

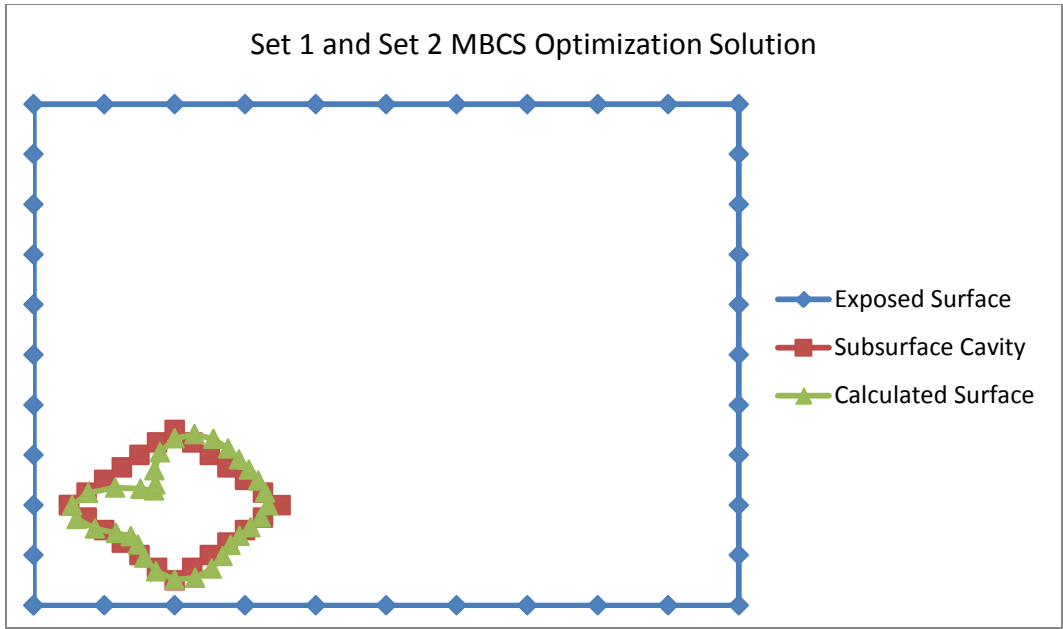


Figure 40: Case 10 two set MBCS optimization solution

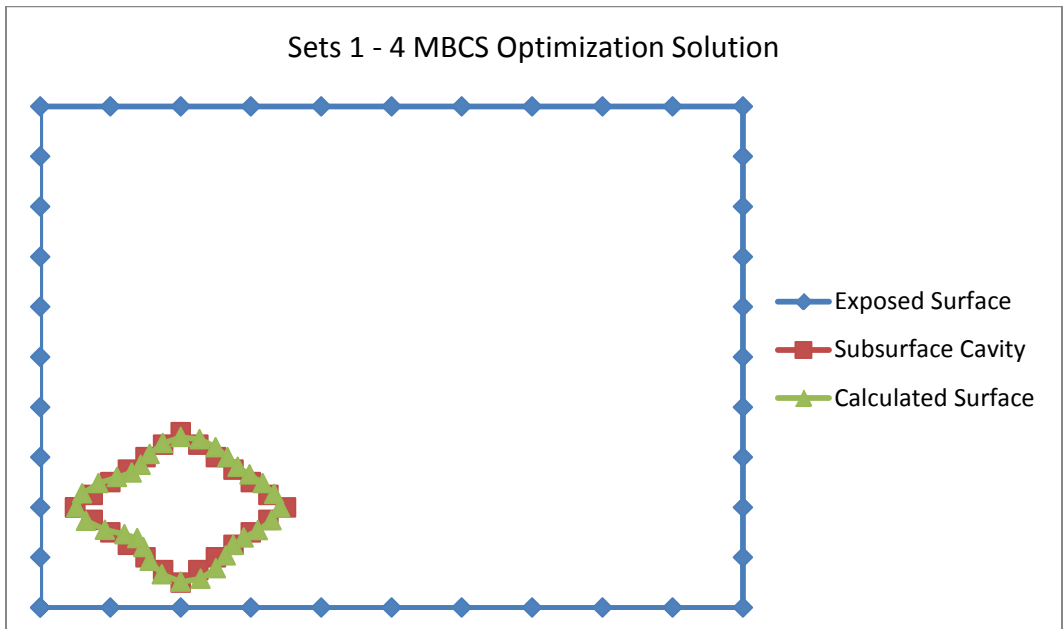


Figure 41: Case 10 four set MBCS optimization solution

CONCLUSION

An automated algorithm for detecting cavities and reconstructing their shape has been successfully tested and used in hypothetical experiment setups. Boundary element code testing methods have also been explored and used to check the solver code used in these solutions. Constant elements were also proven to be accurate enough to detect the shape of the cavity through optimization by increasing the resolution of the boundary elements. Single and multiple cavity problems were introduced with simple and complex geometries to test the performance of the automated system. The system performed to expectations by successfully increasing the resolution of subsurface cavity geometry prediction. Multiple boundary condition set optimization also succeeded in increasing the resolution of the problem without adding boundary elements to the surface. Complicated cavity geometry and location difficulties have proven to be avoidable with MBCS. These techniques can be extended to 3-D geometries, and shows promising calculation speeds due to the low parameter counts being optimized.

Unknown boundary conditions on the subsurface cavities were also explored in case 7 of this article, and proved to be troublesome for the Nelder-Mead simplex method. A more robust optimizer should be used in these unknown boundary condition problems to yield accurate results. The question of a unique solution arises in these problems, but they have been solved by adding penalty functions to the least squares functional.

REFERENCES

- [1] A. J. Kassab and J. Pollard, Cubic Spline Anchored Grid Pattern Algorithm for High Resolution Detection of Subsurface Cavities by the IR-CAT Method, *Numerical Heat Transfer B*, vol. 26, no. 1, pp. 63-78, 1994.
- [2] E. Divo, A. J. Kassab and F. Rodriguez, An Efficient Singular Superposition Technique for Cavity Detection and Shape Optimization, *Numerical Heat Transfer B*, vol. 46, pp. 1-30, 2004.
- [3] A. J. Kassab, F. A. Moslehy and A. B. Daryapurkar, Nondestructive Detection of Cavities by an Inverse Elastostatics Boundary Element Method, *Engineering Analysis with Boundary Elements*, vol. 14, pp. 45-55, 1994.
- [4] D. Ojeda, E. Divo and A. J. Kassab, Cavity Detection in Biomechanics by an Inverse Evolutionary Point Load BEM Technique, *Inverse Problems in Science and Engineering*, vol. 16, no. 8, pp. 981-993, 2008.
- [5] A. Karageorghis, D. Lesnic and L Marin, A Moving Pseudo-boundary Method of Fundamental Solutions for Void Detection, *Wiley Online Library*, 10.1002/num.21739, 2012
- [6] A. Karageorghis, D. Lesnic and L Marin, The Method of Fundamental Solutions for the Detection of Rigid Inclusions and Cavities in Plane Linear Elastic Bodies, *Computers and Structures*, vol. 106-107, pp. 176-188, 2012.
- [7] A. Karageorghis, D. Lesnic and L Marin, A Survey of the MFS to Inverse Problems, *Inverse Problems in Science and Engineering*, vol. 19, no. 3, pp. 309-336, 2011
- [8] C. A. Brebbia and J. Dominguez, *Boundary Elements an Introductory Course*, CMP, Great Britain, 1992.
- [9] E. Divo and A. Kassab, *Boundary Element Method for Heat Conduction: with applications to non-homogeneous media, Anisotropic Heterogeneous Heat Conduction*, Wessex Institute of Technology Press, Southampton, 2003.
- [10] W. H. Press, S. A. Teukolsky and W. T. Vetterling, *Numerical Recipes in FORTRAN 77*, CUB, Cambridge, 2001
- [11] A. Kassab, E. Divo and D. Pepper, *Boundary Element Methods*, ASME Press, In Print, New York, 2013.

- [12] G. S. Gipson, *Boundary Element Fundamentals: Basic Concepts and Recent Developments in the Poisson Equation (Topics in Engineering)*, Wessex Institute of Technology Press, Southampton, 1987.
- [13] A. Bejan, *Heat Transfer*, JWS, New York, 1993
- [14] M. Ozisik, *Heat Conduction*, edi. 2, JWS, New York, 1993